Understanding Polarization Accuracy: The effect of dielectric mirror coatings on instrument polarization behavior at a system level

by

Amanda J. White

B.S., Drexel University, 2011

M.S., University of Colorado, Boulder, 2018

A thesis submitted to the

Faculty of the Graduate School of the

University of Colorado in partial fulfillment

of the requirements for the degree of

Doctor of Philosophy

Department of Astrophysical and Planetary Sciences

2023

Committee Members:

David Harrington

Zachory Berta-Thompson

Steven Cranmer

Robert McLeod

Thomas Schad

White, Amanda J. (Ph.D., Astrophysical and Planetary Sciences)

Understanding Polarization Accuracy: The effect of dielectric mirror coatings on instrument polarization behavior at a system level

Thesis directed by Dr. David Harrington

In astronomy, the ability to make in situ measurements is rare and incredibly limited. As many physical inferences as possible are squeezed out of every photon observed by astronomers, making the resulting models and theories only as good as the data collected and the methods used to calibrate those data. As science requirements drive tighter constraints on the sensitivity and accuracy of measurements, calibration efforts must also be improved.

Astronomical mirror coatings are often metals protected by multiple layers of dielectrics. Varying the thickness and layering of the dielectrics can lead to significant changes in the polarization properties (retardance, diattenuation, and depolarization) of reflected light across all wavelengths. The polarized response also varies with the angle of incidence, the shape of the mirror, and the uniformity of the coating. In models that predict the polarized response of simple or complex optical systems, assumptions are usually made on the properties and uniformity of coated optical surfaces.

The National Science Foundation's Daniel K. Inouye Solar Telescope (DKIST) aims to take polarization measurements of unprecedented polarimetric sensitivity and accuracy in order to achieve its science goals. This requires detailed knowledge of all sources of instrumental-induced polarization changes, particularly from the various coatings on optics, to accurately predict both polarization performance through the entire DKIST system in all possible configurations, and to predict any polarization errors across the telescope field of view.

This thesis seeks to improve current polarization calibration methods by characterizing different dielectric mirror coatings and providing more realistic inputs to the system models being used. We first assess the impact of refractive index source data on the accuracy of model outcomes.

We then present how a non-uniformly applied coating affects polarization performance and causes depolarization across an aperture. Using DKIST as an application, we compare the depolarization effects of mirror coating non-uniformity to other known sources of systematic polarization error. We find for the majority of wavelengths that estimates of depolarization are well within the tolerance limits set by DKIST's error budget. However, the depolarization estimates at the 396 nm and 854 nm Ca II lines were found to be on the order of 10^{-2}, which is *above* the allowed tolerance for error in DKIST *without* accounting for any other sources of systematic error. We conclude that more work is needed at the Ca II wavelengths to determine if DKIST's current wavelength-independent error matrix is sufficient for understanding polarization accuracy requirements across the entire DKIST wavelength bandpass or if a wavelength-dependent error matrix must be developed for the best prediction of system performance.

In the reflecting telescope, the mirror's the thing.
No matter how elaborate and accurate the rest of the
instrument, if it has a poor mirror, it is hopeless.

Russel W. Porter[1]

Dedication

For those who taught me what it means to be **"Unbroken."**

Land Acknowledgement

We acknowledge that the National Science Foundation's Daniel K. Inouye Solar Telescope is located on land of spiritual and cultural significance to Native Hawaiian people. The use of this important site to further scientific knowledge is done so with appreciation and respect. We are honored to have the opportunity to conduct astronomical research on Haleakalā on the Island of Maui in Hawaií. We recognize and acknowledge the very significant cultural role and reverence that this site has to the Native Hawaiian community. We also acknowledge the cultural devastation caused by the overthrow and later annexation of the Kingdom of Hawaií that still pervades the Islands and its Native Hawaiian people today.

We also acknowledge that the University of Colorado Boulder and the National Solar Observatory's Boulder Headquarters are located upon land within the traditional territories and ancestral homelands of the Cheyenne, Arapaho, and Ute Nations. Further, we acknowledge the 48 contemporary tribal nations historically tied to the lands that comprise what is now called Colorado. With this land acknowledgment, we celebrate the many contributions of Native peoples to the fields of medicine, mathematics, astronomy, arts, literature, engineering and more.

We recognize and affirm the ties these nations have to their traditional homelands and the many Indigenous people who thrive in these places, alive and strong. We acknowledge the painful history of ill treatment and forced removal that has had a profoundly negative impact on Native nations. While we can never undo or rectify the devastation wrought on Indigenous peoples, we commit to improving and enhancing engagement with Indigenous peoples and issues both locally and globally.

Acknowledgements

There are many people without whom this work would not exist. Your input and support has been invaluable to me whether or not you realized it. Special thanks are needed for:

Beekey, thank you for letting me drag you across the country and then subject you to all the emotional ups and downs of graduate school. I am so grateful that you have supported all of my side quests and have always been there to literally pick me up off the floor when I am down, usually with a pint of ice cream at the ready.

Lincoln and Orion, my support dogs who always made sure that I had company and snuggles during the latest of nights. Thank you for knowing when, and how, to shut a laptop lid when I did not. I am still not sure who taught you that, but you are the bestest boys.

Dave, thank you for, as you put it, “going on this crazy ride” of paperwork and never ending employment status snafus. Thank you for taking a chance on me after I randomly showed up at your desk, even though I didn’t listen to any of your advice on grad school so many years earlier.

Arika, you are the biggest reason I actually finished this dissertation. Thank you for believing in me even when I didn’t, for pulling me back every time I quit, and for spending so much time body doubling with me. You are an amazing friend. You are the absolute best.

Everyone at Uplift, from the coaches to the members, thank you for being, well, so uplifting. The gym has become a special place of solace and support through so much stress. A special shout-out to Jena for being a wonderful coach and an even better friend. Thank you for being my unwavering cheerleader and non-academic sounding board. Thank you for reminding me there is more out there than work and for introducing me to so many amazing pups. If only everyone could

be so lucky as to have you shout “KNEES!!” at them from across the room.

There are many others, but to keep it short, I thank everyone who made my time in Colorado bearable. Thanks to my fellow graduate students, especially Liz B., Aylecia L., Eryn C., Nicole A., Alex H., Ryan D-P., Sam W., and Emily W. To the APS faculty for their support, especially David Brain, Nils Halverson, Phil Armitage, and Zach Berta-Thompson. And finally, many thanks to those at NSO who kept me engaged with the Boulder office throughout the pandemic, especially Kevin Reardon, Gianna Cauzzi, and Claire Rafferty.

I have also been very lucky to have received financial support for the majority of my graduate studies. Thank you to the George Ellery Hale Fellowship program which funded three years of my tenure at CU and allowed me to work at NSO with Dave. I am also grateful to the DKIST construction project and its associate director, Thomas Rimmele, for funding my work both before and after the Hale Fellowship.

Contents

Chapter

Tables

Table

Figures

Figure

Chapter 1

Introduction

In astronomy, in situ measurements, for the most part, cannot be made. With few exceptions, such as finding meteorites, sending a return sample mission to space, or plunging a space probe into the atmosphere of a planet, it is impossible to bring pieces of the Universe into an Earth laboratory. Instead, we are left to infer the physical properties of a celestial object from the observables that we *can* measure, specifically the intensity and wavelength of light.[2–4] Through imaging, photometry, spectroscopy, interferometry, polarimetry, and the myriad of other observational techniques available to modern astronomers, we are able to squeeze as many physical inferences as possible out of every single photon observed. However, the resulting models and theories can only be as good as the data collected. And errors are lurking around everywhere, propagating through the instrumentation and into the data.

This thesis seeks to improve current polarization calibration methods by providing more realistic inputs to the system models being used in the calibrations. The following introductory chapter will provide the reader with an abridged background in polarization (Section 1.1), how it is measured (Section 1.2), and where polarization is found (Section 1.3). This chapter will also introduce the reader to different types of optical coatings and how the manufacturing process affects the resulting optic and its polarization (Section 1.4). Finally, the reader will be introduced to the National Science Foundation's Daniel K. Inouye Solar Telescope (DKIST) as the motivation for this study in Section 1.6.

The Science chapters of this thesis will assess specific error sources on system modeling efforts through the use of metrology and reassessing what can and cannot be ignored as polarimetry reaches new levels of precision and accuracy requirements. Chapter 2 details the importance of modeling the refractive index of an individual optical coating. Two optics manufactured with identical coating formulas and deposition methods in the same coating chamber may have distinct polarization properties. Chapter 3 explores the loss of polarization by an optic due to non-uniformly applied coatings. Depolarization is often ignored in instrument system models and this chapter will also analyze if it is acceptable for depolarization of mirrors to be omitted when there are many sources of polarization error. Chapter 4 builds on Chapter 3 by incorporating more complexity. Here we examine how multiple optics, angles, and rotations further impact instrument-induced polarization. Chapter 5 rounds things out with a look at what implications there are for DKIST and other telescopes, as well as future directions.

1.1 Polarization of Light

Polarization is a fundamental property of light that describes the direction of propagation of the electric field vector of a transverse electromagnetic wave.[4–7] If the orientation of the electric field vector is in a single plane, with the field oscillating in a single direction, the light is linearly polarized as in Figure 1.1. Similarly, if the amplitude of the electric field vector remains constant but the direction of the vector is rotating at a constant rate about the axis of propagation, the light is circularly polarized. If there is no correlation between the direction of the electric field vector over time and it is randomly distributed about the axis of propagation, the light is unpolarized. Light can also be in a superposition of polarized and unpolarized states which is described as partially polarized.[4,5]

1.1.1 The Polarization Ellipse

From the detection of electromagnetic energy and Maxwell's equations, a tensor description of the polarization of a monochromatic wave can be derived.[4,5,7,8] Known as the coherency matrix ($\mathbf{C}$) or the polarization tensor, the tensor in Equation 1.1 characterizes both the energy and propagation

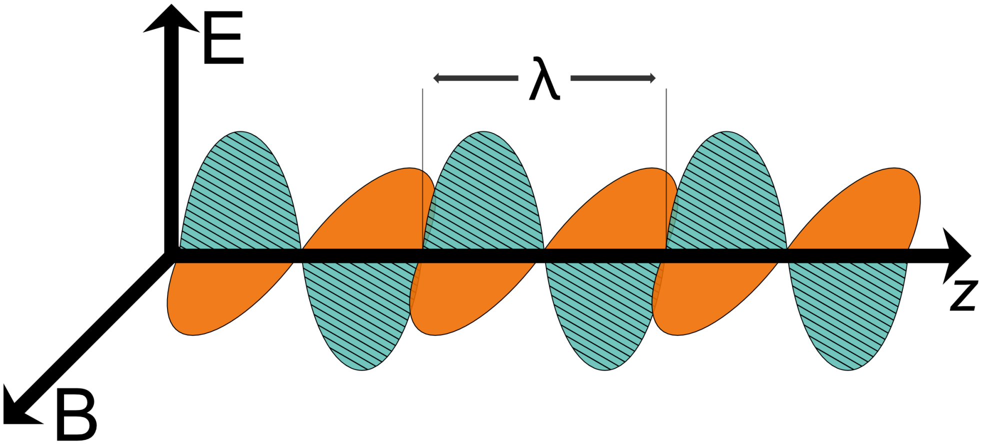

Figure 1.1: A transverse electromagnetic wave. The direction of wave propagation is perpendicular to the oscillations of both the electric (green, striped) and magnetic fields (orange), which are also perpendicular to each other. As the electric field vector is constrained to oscillate in a single plane (vertically), this is an example of a linearly polarized wave.

properties of an electromagnetic wave.

$$\mathbf{C} \equiv \begin{pmatrix} E_x E_x^* & E_x E_y^* \\ E_y E_x^* & E_y E_y^* \end{pmatrix} \tag{1.1}$$

where E_x and E_y are orthogonal components of the electric field E and * denotes the complex conjugate.

Using the plane wave solution of the homogeneous wave equation ($E_j = a_j e^{-i(\omega t - \delta_j)}$), the coherency matrix can be rewritten as:

$$\mathbf{C} = \begin{pmatrix} a_x^2 & a_x a_y e^{i\delta} \\ a_x a_y e^{-i\delta} & a_y^2 \end{pmatrix} \tag{1.2}$$

where a is the real component of the amplitude and

$$\delta \equiv \delta_x - \delta_y \tag{1.3}$$

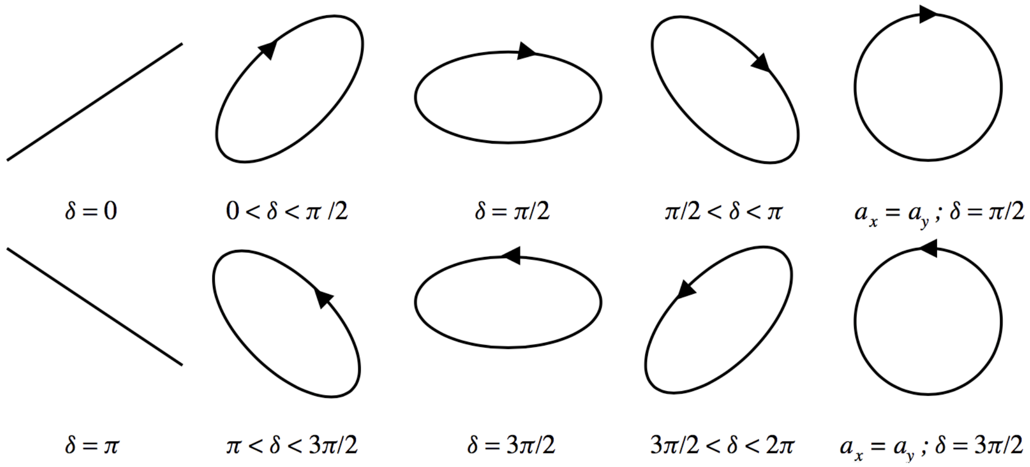

Figure 1.2: Examples of possible states for totally polarized radiation for different values of the phase difference δ. When δ is equal to 0 or π, the ellipse becomes a straight line and the radiation is linearly polarized as shown in the first column. When the amplitudes of the intensity are equal ($a_x = a_y$), and $\delta = \pi/2$ or $\delta = 3\pi/2$, the ellipse becomes a circle and is circularly polarized as in the last column. *Reproduced from Fig. 2.3 of Introduction to Spectropolarimetry (del Toro Iniesta 2003).*[8]

is the constant phase difference between the x and y components of the electric field vector.[4,5,7–9]

If we treat the electromagnetic wave components E_x and E_y as a superposition of two oscillating waves, we can see that the diagonal elements of Equation 1.2 are proportional to the real intensities of these waves. The sum, or trace, of the diagonal, $\mathbf{T}(\mathbf{C})$, is then the total intensity of the electromagnetic wave and can be used to trace out an ellipse which is described by four parameters; E_x, E_y, δ_x, δ_y. Furthermore, different orientations of the ellipse occur for different phase differences (δ) and the different signs of δ as shown in Figure 1.2.[4,5,8–10]

1.1.2 Describing the polarization properties of optics

The polarization properties of a given optical element can be characterized by three general properties: diattenuation, retardance, and depolarization.

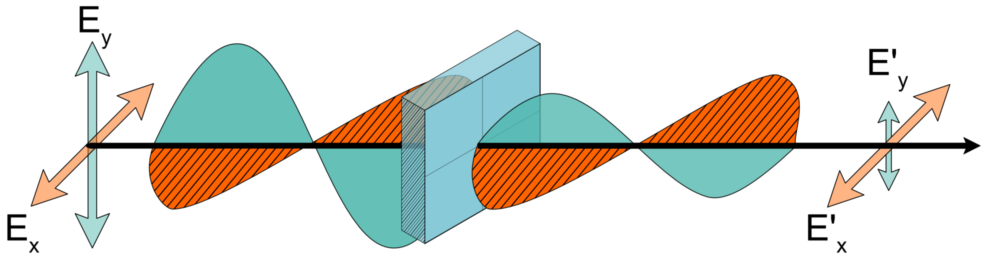

Figure 1.3: Diattenuation occurs when there is a change in amplitude of one component of the electric field. Light propagates from left to right in the diagram and enters a polarizer with equal amplitudes in the $\mathbf{E}_x$ and $\mathbf{E}_y$ planes. The light wave exits the polarizer with the same amplitude, $\mathbf{E'}_x = \mathbf{E}_x$, on the horizontal axis, and with a smaller amplitude, $\mathbf{E'}_y$, on the vertical axis. In this example, the new amplitude of $\mathbf{E'}_y$ has been attenuated, while $\mathbf{E'}_x$ has been preserved.

Diattenuation

Diattenuation occurs when the orthogonal amplitudes of the electric field components of a light wave change unequally. It is used to indicate the strength of a diattenator optical element. For example, a polarizer that only allows components of the electric field that are aligned with the transmission axis to pass through the optic is a diattenuator. Figure 1.3 represents this pictorially: as a transverse light wave propagates from left to right, it starts with equal amplitudes in the $\mathbf{E}_x$ and $\mathbf{E}_y$ planes. As the wave passes through a polarizer, the amplitude of the $\mathbf{E}_y$ component decreases. However, the $\mathbf{E}_x$ component remains unchanged.

Diattenuation, D, can be quantified using the maximum and minimum transmittance values over all polarization states.[4,5] It is defined as:

$$D = \frac{T_{Max} - T_{Min}}{T_{Max} + T_{Min}},\ 0 \leq D \leq 1 \tag{1.4}$$

with $D = 1$ being an ideal polarizer and $D = 0$ indicating that an optic transmits light with equal attenuation independently of the incident polarization state.

In the real world, it is very difficult to manufacture an optic with zero diattenuation. It is

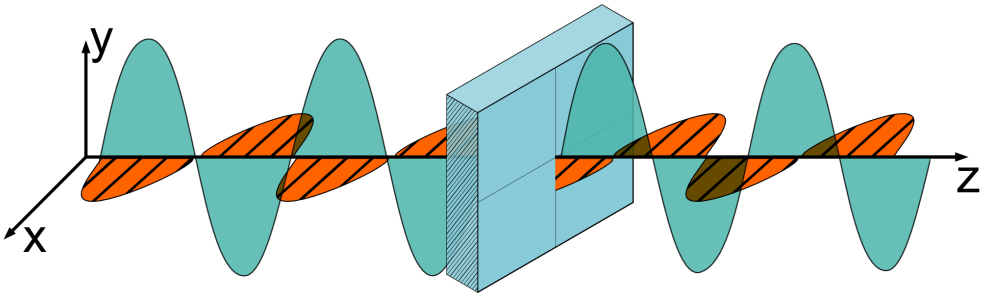

Figure 1.4: Retardance occurs when there is a phase difference between the X and Y components of the electric field. This transverse wave enters a retarder with its striped and solid components in phase. The exiting wave is no longer in phase with the striped component lagging behind the solid component. The optic has retarded the wave in the X plane.

possible to get very close to zero but not $D = 0$ (or very close to $D = 1$ but not exactly, for that matter); however, almost all optics will have some diattenuation. A portion of Chapter 2 will look at the impact of even a small amount of diattenuation.

Retardance

Retardance, δ, refers to a phase difference between the $\mathbf{E}_x$ and $\mathbf{E}_y$ components of the electric field. An optic that changes the phase difference of a polarized wave is known as a retarder as demonstrated in Figure 1.4. This is usually due to two different refractive indices, such as the ordinary and extraordinary optical axes of a birefringent crystal. Regardless of the polarization input state (i.e. the field does not need to be in phase), retardance is measured from the phase difference between the input and output polarization state and is a property of the optic. Many retarders are described in waves, radians, and degrees interchangeably. For example, a half-wave linear retarder has a retardance of $\delta = \pi$ radians or 180°. Similarly, a quarter-wave linear retarder imparts $\delta = \frac{\pi}{2}$ or 90° phase difference on any input polarization. This thesis will report all retardance values in units of degrees.

Depolarization

The third descriptor used is depolarization, or the reduction of the Degree of Polarization (DoP) of polarized light. Any randomization of the average polarization over an aperture is depolarization. DoP is defined as:

$$DoP(\mathbf{S}) = \frac{\sqrt{S_1^2 + S_2^2 + S_3^2}}{S_0}, 0 \leq DoP \leq 1 \tag{1.5}$$

where S is the incoming Stokes vector. A DoP of 1 indicates that the light is fully polarized; likewise, a DoP of 0 is unpolarized light, and anything in between is partially polarized.

1.1.3 Stokes Vectors

As described in the previous section, the diagonal elements of the coherency matrix (Equation 1.2) represent the real amplitudes of the x and y components of the electric field. The off-diagonal elements represent the complex spatial exponentials which are not directly observable. Because we cannot measure the complex elements of the coherency matrix, we instead form a linear combination of the real elements that *can* be measured.[8] These are the so-called Stokes parameters and are given by:

$$\begin{aligned} I &= \kappa(a_x^2 + a_y^2) \\ Q &= \kappa(a_x^2 - a_y^2) \\ U &= 2\kappa a_x a_y \cos\delta \\ V &= 2\kappa a_x a_y \sin\delta \end{aligned} \tag{1.6}$$

where κ is a dimensional constant translating the parameters into intensity units. a_x, a_y, and δ represent the amplitudes and constant phase difference of the components of the electric field in Equation 1.2.

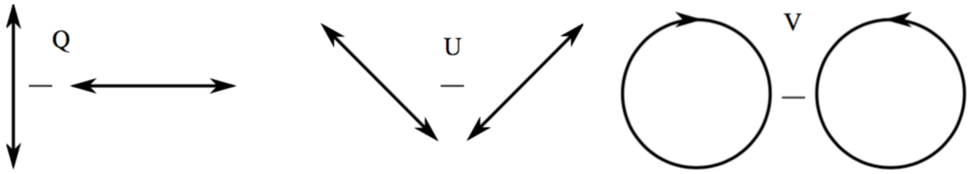

Figure 1.5: The polarized elements of a Stokes vector. Q and U both represent linear polarization while V describes the circular polarization. The squared sum of the elements sums to the total intensity I in Equation 1.8

For easy computation, Stokes parameters are commonly arranged into a column matrix referred to as the Stokes vector:

$$S = \begin{bmatrix} S_0 \\ S_1 \\ S_2 \\ S_3 \end{bmatrix} = \begin{bmatrix} I \\ Q \\ U \\ V \end{bmatrix} \tag{1.7}$$

and

$$I^2 \geq Q^2 + U^2 + V^2 \tag{1.8}$$

where I is the overall intensity of the radiation, ± Q (at 0° and 90°) and ±U (at ±45°) describe the linear polarization and ±V the circular polarization. For fully polarized light, Equation 1.8 becomes an equality statement while partially or unpolarized light is represented by the inequality statement. Figure 1.5 pictorially shows the orientation of each parameter. In this form it is easy to see how Stokes parameters are able to be measured as they are real quantities, directly related to intensity.[2,4–8,10,11]

1.1.4 Mueller Matrices

The polarization state of light will almost always change from interactions with matter.[5,8] The 4×4 transfer matrix that describes the propagation of polarization through an optical element is known as a Mueller matrix. Each matrix element describes how an input Stokes vector is changed into a Stokes output vector and must satisfy the equation

$$\mathbf{S}_{out} = \mathbf{M}_{ij}\mathbf{S}_{in} \tag{1.9}$$

where $\mathbf{M}_{ij}$ is the Mueller Matrix:[5,7,12,13]

$$\mathbf{M}_{ij} = \begin{pmatrix} II & QI & UI & VI \\ IQ & QQ & UQ & VQ \\ IU & QU & UU & VU \\ IV & QV & UV & VV \end{pmatrix}. \tag{1.10}$$

Every optical element can be described by a Mueller matrix, and each matrix element describes how an input Stokes vector is transferred into a Stokes output by the optic. For example, using the notation of Equation 1.10, the QI term denotes how incoming linear polarization in the Q direction is converted into intensity, I.

Experimental Mueller matrices can be further decomposed into separate terms for diattenuation, retardance, and depolarization terms with various decomposition schemes.[5,14] Diattenuation occurs when the orthogonal amplitudes of an optical beam change unequally. A polarizer that only allows waves aligned with the transmission axis to pass through is an example of a diattenuator. Retardance refers to the phase shift of one orthogonal state relative to the other, such as the shift that could be caused by a quarter-wave plate.

To describe a single flat-fold mirror with a standard Mueller matrix, three quantities are needed: the reflectivites perpendicular (R_s) and parallel (R_p) to the plane of incidence and the phase change due to retardance (δ). We can then infer the transmission and diattenuation of the mirror directly from the Mueller matrix as in Equation 1.11:

$$\mathbf{M}_{ij} = R_{avg} \begin{pmatrix} 1 & \frac{R_s - R_p}{R_s + R_p} & 0 & 0 \\ \frac{R_s - R_p}{R_s + R_p} & 1 & 0 & 0 \\ 0 & 0 & 2\frac{\sqrt{R_p R_s}}{R_s + R_p} C_\delta & 2\frac{\sqrt{R_p R_s}}{R_s + R_p} S_\delta \\ 0 & 0 & -2\frac{\sqrt{R_p R_s}}{R_s + R_p} S_\delta & 2\frac{\sqrt{R_p R_s}}{R_s + R_p} C_\delta \end{pmatrix} \tag{1.11}$$

where R_{avg}, the average reflectivity of the mirror, is equivalent to the transmission. Assuming the optic is oriented such that it is tilted in the Q plane, the Mueller matrix can be further approximated as:

$$\mathbf{M}_{ij} \sim \begin{pmatrix} 1 & \Delta & 0 & 0 \\ \Delta & 1 & 0 & 0 \\ 0 & 0 & C_\delta & S_\delta \\ 0 & 0 & -S_\delta & C_\delta \end{pmatrix}. \tag{1.12}$$

The QI and IQ terms in the first row and in the first column are representative of diattenuation (Δ). C_δ and S_δ are used to denote $\cos\delta$ and $\sin\delta$, respectively, in the UV terms of the lower 2×2 matrix within the Mueller matrix. In this form, retardance can be straightforwardly computed as:

$$\delta_{avg} = \frac{\tan^{-1}\frac{VU}{VV} + \tan^{-1}\frac{UV}{UU}}{2}. \tag{1.13}$$

1.2 Polarimetry

Polarization naturally occurs through a variety of different phenomena. Any interaction of a light wave; scattering, reflection, transmission, etc., poses the possibility for the wave's polarization state to change. Examples range from the scattering of light in the daytime sky to the birefringence of scarab beetles.[5,7,15] Polarimetery refers to the measurement of such phenomena using polarization elements to determine the retardance, diattenuation, and depolarization of a light wave. Spectropolarimetry is "the measurement of light that has been analyzed both spectroscopically and polarimetrically".[8] Spectropolarimetry utilizes the wavelength-dependent polarization state of a light source to determine information about the source beyond what information the intensity alone provides, such as constraints on the geometric structure of the source.[16] For example, if both unpolarized and linearly polarized light are detected from a star that also shows evidence of circumstellar material, an observer may conclude that the excess material has somehow flattened and a circumstellar disk exists. The material cannot be spherically distributed because it is emitting linear polarization.[16] Another example of spectropolarimetry at work is often used by those studying the magnetic field of a stellar atmosphere. When the absorption spectrum of certain atomic lines is examined, the presence, strength, and dynamical properties of a magnetic field can be inferred.[2, 8, 10] This is possible due to the structure of atoms.

1.3 Polarization in the wild - the physics

In an astrophysical setting, most polarization changes are connected to the presence of an external field, such as Zeeman splitting or the Hanle effect. The fine and hyperfine structures of atoms due, respectively, to magnetic and nuclear magnetic dipole moments also produce polarization signatures of import in the study of astrophysical plasmas, as do any form of an anisotropy in an atomic system.[10]

1.3.1 Atomic Lines

Spectral lines have commonly been observed to be polarized in analysis of several astronomical objects. In general, the line polarization signature shows variation along a line profile and may or may not be accompanied by polarization of the continuum.[11] The description of polarization stemming from phenomena of astrophysical interest requires a combination of a Stokes parameter description of the radiation field as well as a description of how the atomic system interacts with the radiation field. Much of this theoretical description can require the derivation of the density-matrix elements which describe the coherence or phase interference between different magnetic sublevels.[2, 11]

1.3.2 Zeeman Effect

In atomic physics, an external uniform magnetic field can be described as a perturbation to the Hamiltonian of the system. The magnetic perturbation can be given by the equation:

$$H_B = \frac{e^- h}{4\pi m_e c}(\vec{L} + 2\vec{S}) \cdot \vec{B} = \mu_0(\vec{L} + 2\vec{S}) \cdot \vec{B} \tag{1.14}$$

where $\vec{L}$ is the total orbital angular momentum, $\vec{S}$ is the total spin angular momentum of electrons, and μ_0 refers to the Bohr magneton.[10] Much of the perturbation comes from the difference in the strength of the internal L-S coupling of the orbital and spin angular momentum and the strength of the external field.

The Zeeman effect refers to the splitting of a spectral line in the presence of a weak magnetic field. It was first observed in a laboratory measurement by Pieter Zeeman in 1896 as a broadening of Sodium D spectral lines. Had Zeeman's spectrograph had more resolving power, he would have observed the sodium D lines splitting rather than broadening.[5] This splitting was predicted by Lorentz but would not be confirmed or fully explained until the advent of quantum mechanics.

This splitting of spectral lines occurs because the external magnetic field breaks the degeneracy of different energy states.

$$\lambda_{J_u - J_l} = \lambda_0 - (m_u g_u - m_l g_l)\Delta\lambda_B \tag{1.15}$$

$$\Delta\lambda_B = 4.6686 \times 10^{-10} \lambda_0^2 \vec{B} \tag{1.16}$$

As shown in Equation 1.15, the emitted wavelength is a combination of the unperturbed wavelength, the angular momentum quantum number m, and the Landé g factor of the energy states involved. We can then use Equation 1.16 and the Larmor frequency to solve for the strength of the magnetic field $\vec{B}$. In this equation. $\Delta\lambda$ is in units of milli-angstroms (mÅ) , λ_0 in angstroms (Å), and $\vec{B}$ in Gauss (G).[10]

The Zeeman effect manifests in the Stokes parameters of an observed spectral feature. For very strong magnetic fields, Zeeman splitting may appear in the intensity spectrum directly, however, it is often the case that it does not appear at a resolvable level. In these cases, polarization measurements of the Stokes Q, U, V are required to differentiate the atomic energy levels.

1.4 Anatomy of a mirror coating

Most mirrors today are coated with thin films. Films are considered thin when the interference between the film and substrate material can be detected coherently.[17] Mirrors in your home are most likely a sheet of glass with a thin layer of silver deposited on the backside, which is then, maybe, protected with a layer of paint. This type of mirror, known as a secondary-surface-mirror, is great for everyday uses as the glass protects the reflective surface from deteriorating. Although easily manufactured and durable, secondary-surface mirrors are not ideal for high-precision optical applications. Incident light first refracts off the exposed glass surface before reflecting off the mirrored surface, as illustrated in Figure 1.6a. The light then refracts again as it exits the glass. At each material interface, incident light loses intensity and gains possible aberrations. Ghost image reflections and internal reflections will appear at the air-glass surface. In certain wavelength bands, glass is absorptive and blocks part of the spectrum from propagating.[7,18,19]

Applications that require high image quality or precision measurements typically use first-surface mirrors instead of secondary-surface mirrors. As shown in Figure 1.6b, incident light reflects directly off the exposed coating surface. What this type of mirror gains in lack of distortions, they lose in durability. First-surface metal coatings (e.g. aluminum, silver, gold, etc.) are often difficult to adhere to a glass substrate, making them very easily damaged.[18] These mirrors either need to be re-coated often or protected from environmental factors. To achieve that, dielectric thin films are deposited as a protective top coat and/or added as an adhesion layer between the metal and the substrate in what is known as a protected coating or an enhanced coating. Dielectric thin films tend to harden more than metallic thin films, making them more resistant than metal alone to mechanical degradation (e.g. scratches) and the effects of the environment.[17]

An example of a protected silver coating is depicted in Figure 1.7. One or more dielectrics are layered over the metal with alternating high to low refractive indices. At a quarter-wave layer

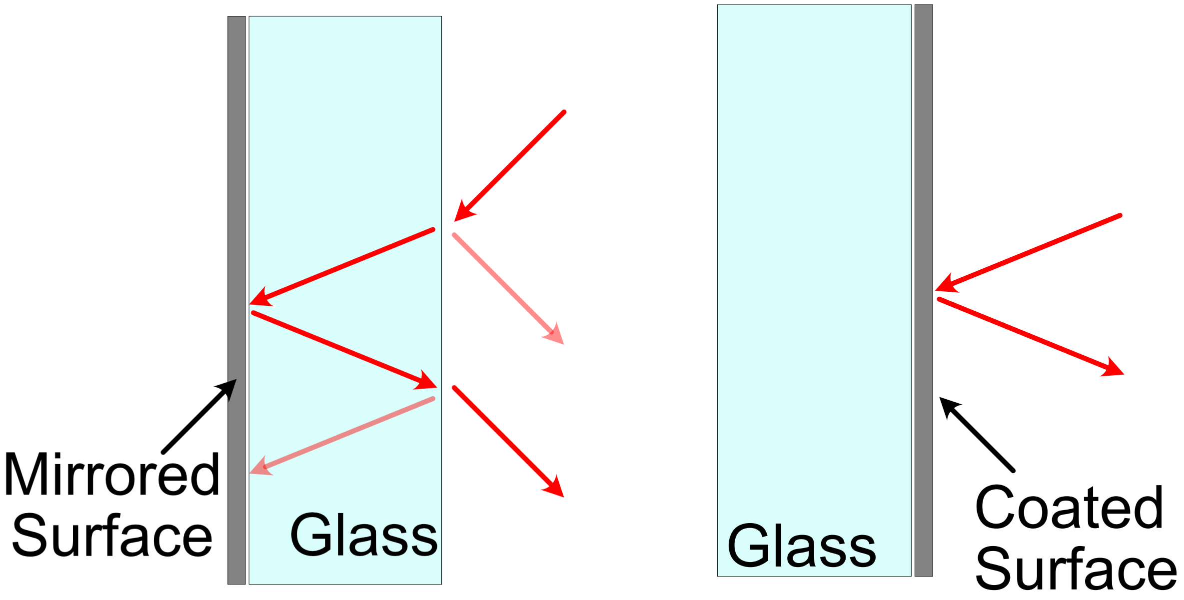

(a)

(b)

Figure 1.6: Mirrored surfaces can either be protected by a substrate as illustrated in **a)** or have the coated surface exposed as illustrated in **b)**. In both panels, the red arrows represent the path of incident light. The exposed glass of a secondary surface mirror refracts the incoming light, adding internal reflections, image ghosting, and other aberrations. For applications that require optical precision, a first surface mirror is preferred as incident light is reflecting directly off of the coating. In this type of design, the coated surface is exposed and light does not reach the glass substrate. A first surface mirror is often desirable for technical applications that are sensitive to absorption by the substrate or wavefront distortions, however some durability is sacrificed.

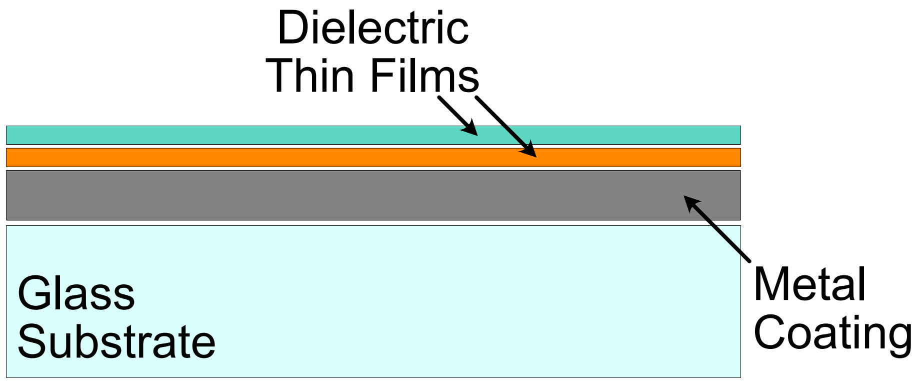

Figure 1.7: Enhanced mirror coatings use various dielectric thin films to boost the performance and durability of first-surface mirrors. Layers of alternating high- and low-refractive-index films protect from environmental damage. A thin adhesive layer deposited before the reflective metal helps the coating to better adhere to the substrate. *Image not drawn to scale.*

thickness, all reflections at layer interfaces will remain in phase and constructively combine at the optical surface. The layers are also designed to be thin enough, a fraction of a wavelength, to not compromise performance due to refraction as in the second-surface mirrors and even boost reflectivity in some formulas when the reflections constructively combine.[18]

1.4.1 Deposition methods

There are many different processes for depositing mirror coatings. The most commonly used methods are electron beam evaporation (e-beam), ion assisted deposition (IAD), and ion beam sputtering (IBS) which are illustrated in Figure 1.8. Each of these three methods has a different effect on the final properties of the coating, such as density, thickness, durability, and peak transmission wavelength, which in turn affects the coating's polarization behavior. E-beam dielectric coatings are manufactured by heating the coating material in a vacuum chamber until it evaporates by bombarding it with electrons. The vaporized coating is then allowed to "waft" towards the ceiling of the coating chamber, where the substrate material is held on a rotating platform. The vaporized coating then recondenses as a film on the glass substrate. Many e-beam coatings exhibit a columnar molecular structure similar to Figure 1.9a. This technique generally

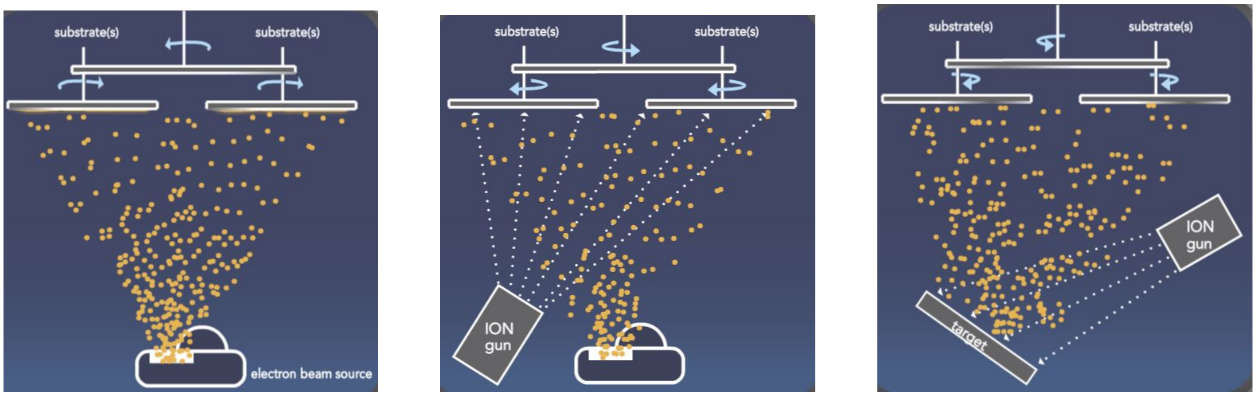

(a) E-Beam and Thermal Evaporation

(b) Ion Assisted Deposition

(c) Ion Beam Sputtering

Figure 1.8: The most commonly used methods for manufacturing thin film coatings are: **a)** Electron Beam Evaporation which heats a source material until it vaporizes and recondenses on the substrate surface; **b)** Ion Assisted Deposition is similar to electron beam evaporation with the addition of a high energy ion gun used to create denser coatings; **c)** Ion Beam Sputtering utilizes high energy ions to free atoms from the target source rather than thermal heating. This results in a more precise and uniform coating. *Reproduced from https://www.reoinc.com*[20]

results in a highly porous and less durable coating that can have a high variability of thicknesses between coating runs; meaning that the same coating chamber run on the same settings can produce two non-identical coatings. Even with these drawbacks, e-beam coatings are common because they can span a wide spectrum of ultraviolet to infrared wavelengths and have a relatively low manufacturing cost.[7,17,20]

Coatings manufactured with IAD undergo a process similar to that of e-beam coatings. The coating material is vaporized and allowed to recondense on the substrate surface. As condensation occurs, an ion beam is fired at the substrate to assist with packing of the coating. IAD results in a higher density and more durable coating than what is achieved with only evaporation. Although more durable, the process of ion packing also causes the coating to lose some of its birefringent properties. Coatings that require birefringence are often first deposited with an e-beam method and then sealed with a thin IAD coating for durability such as the one in Figure 1.9b.[7,20]

The most durable and stable of coatings are produced by ion sputtering methods such as IBS. To deposit coatings in this way, a high-energy ion beam is fired at a target made of the coating material. Momentum from the ion beam is transferred to the atoms of the target material that sputter off and are deposited onto the substrate. IBS-produced coatings are very dense, highly uniform, and amorphous in structure. These coatings also typically produce very little scattered light. This is due to very precise deposition, which results in a very low surface roughness. Because of these properties, IBS coatings are ideal for many uses including steep-edge filters, broad- and multi-wavelength mirrors, and antireflection (AR) coatings. Unfortunately, IBS coatings can only be produced with a small subset of materials, mainly metal oxides, which limits the techniques use to a small subset of wavelengths in the optical regime.[20]

1.5 Berreman Calculus

Berreman calculus is a mathematical formalism that is commonly used in the thin film industry. Originally introduced by Teitler & Henvis (1970)[21] as a method of tracing light propagation and reflection through a stratified, anisotropic medium, the technique was later expanded by Dwight

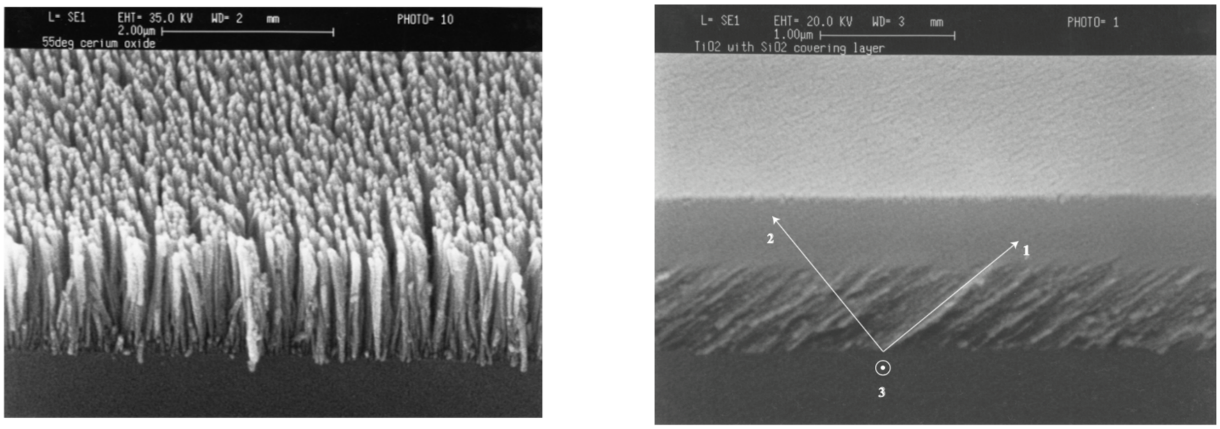

(a) Columnar structure of cerium oxide

(b) Fractured titanium oxide film with columnar structure over coated with a layer of amorphous silicon oxide

Figure 1.9: The molecular structure of a coating is dependent on deposition method, angle of deposition, and environmental factors such as temperature and pressure. Columnar structures grow from e-beam techniques as seen in a. Other methods, such as IAD and IBS, result in amorphous coatings as in the top layer of b. *Reproduced from McCall, Hodgkinson, and Wu, Figures 1.2 and 7.8*[7]

Berreman in 1972 as a way to calculate transmission and reflections of a continuously varying liquid crystal.[22] This section will explain the step-by-step process of using Berreman calculus to calculate the properties of mirror coatings.

Berreman calculus uses a 4 × 4 matrix method to describe how the electromagnetic field components of a transverse wave propagate through a medium. The method is similar to how a Mueller matrix describes the propagation of a Stokes vector; however, what makes the Berreman calculus different from other methods is how general a theory it is. Berreman calculus is capable of following Maxwell's equations through an arbitrarily polarized medium while handling multiple internal reflections, forward and backward propagations, and complex configurations of multiple birefringent layers.[7,22] Both phase and partially polarized or unpolarized fields are handled, which is not true of other matrix techniques. Jones calculus, a 2 × 2 matrix method that describes how an incident light vector will propagate through a sequence of optical elements, is only applicable to fully polarized light propagating through an isotropic medium.[4,23] Mueller matrices, described in Section 1.1.4, track fully polarized, partially polarized, and unpolarized light using Stokes vectors. Unfortunately, Mueller matrices lose the phase information of the electromagnetic field.

In the Berreman formalism, Maxwell's equations for electromagnetic fields are traced by a 4 × 4 transfer matrix through the stack of material being analyzed. Components of the electric E and magnetic H fields form four basis vectors that make up the transfer matrix:

$$\hat{F} = \begin{pmatrix} E_{y1}^{+} & E_{y1}^{-} & E_{y2}^{+} & E_{y2}^{-} \\ H_{z1}^{+} & H_{z1}^{-} & H_{z2}^{+} & H_{z2}^{-} \\ E_{z1}^{+} & E_{z1}^{-} & E_{z2}^{+} & E_{z2}^{-} \\ H_{y1}^{+} & H_{y1}^{-} & H_{y2}^{+} & H_{y2}^{-} \end{pmatrix} \tag{1.17}$$

which is referred to as the field matrix.

Waves propagating through a biaxial medium will be the result of multiple reflections and transmissions and can be described as a linear combination of basis vectors. Propagating waves are represented by a basis vector multiplied by a set of complex field coefficients, $\vec{a}$, of the form:

$$\vec{a} = \begin{bmatrix} a_1^+ \\ a_1^- \\ a_2^+ \\ a_2^- \end{bmatrix}. \tag{1.18}$$

In order for the total field, m, to be conserved across layer interfaces, it must be related to both the field matrix and coefficients. The total field can then be obtained as the field matrix transforms the field coefficients into the total field by

$$\hat{F}\vec{a} = \vec{m}. \tag{1.19}$$

As waves propagate through a biaxial medium, they will most likely gain a phase difference linearly with displacement. The motion can be described by a phase matrix, $\hat{A}_d$ of the form

$$\hat{A}_d = \begin{pmatrix} \exp[-i\phi_1^+] & 0 & 0 & 0 \\ 0 & \exp[-i\phi_1^-] & 0 & 0 \\ 0 & 0 & \exp[-i\phi_2^+] & 0 \\ 0 & 0 & 0 & \exp[-i\phi_2^-] \end{pmatrix}, \tag{1.20}$$

where $\phi^\pm = kn\cos\theta^\pm d$, n is refractive index, θ is angle of incidence, and d is physical thickness of the layer.

Together, the field matrix, $\hat{F}$, and the phase matrix, $\hat{A}_d$, can be used to compute the characteristic matrix of the material

$$\hat{M} = \hat{F}\hat{A}_d\hat{F}^{-1} \tag{1.21}$$

which describes the transformation of the total field between two points in the same material layer. The characteristic matrix is often used to calculate through an entire layer, from one interface to the other, but can be used with any two points. When both interfaces are used to compute the characteristic matrix, the many layers of a medium become multiplicative and the total characteristic matrix can be determined by

$$\hat{M} = \hat{M}_1 \hat{M}_2 \hat{M}_3 .... \hat{M}_N \tag{1.22}$$

We can then rearrange Equation 1.21 into an eigenvalue problem and solve for both $\hat{F}$ and $\hat{A}_d$. The field matrix can then be used with Maxwell's equations for plane, harmonic waves (e.g. $\alpha = -z_0 H_y / E_z$) to construct $\hat{\alpha}$ as

$$\hat{\alpha} = \begin{pmatrix} -z_0 F_{41}/F_{31} & 0 & 0 & 0 \\ 0 & -z_0 F_{42}/F_{32} & 0 & 0 \\ 0 & 0 & -z_0 F_{43}/F_{33} & 0 \\ 0 & 0 & 0 & -z_0 F_{44}/F_{34} \end{pmatrix} \tag{1.23}$$

With both $\hat{F}$ and $\hat{\alpha}$, we can determine the auxiliary matrix, $\hat{L}$,

$$\hat{L}\hat{F} = \hat{F}\hat{\alpha} \tag{1.24}$$

where

$$\hat{L} = \begin{pmatrix} -\frac{\beta \varepsilon_{xy}}{\varepsilon_{xx}} & z_0 - \frac{z_0 \beta^2}{\varepsilon_{xx}} & -\frac{\beta \varepsilon_{xz}}{\varepsilon_{xx}} & 0 \\ \frac{\varepsilon_{yy}}{z_0} - \frac{\varepsilon_{xy}^2}{z_0 \varepsilon_{xx}} & -\frac{\beta \varepsilon_{xy}}{\varepsilon_{xx}} & \frac{\varepsilon_{yz}}{z_0} - \frac{\varepsilon_{xy} \varepsilon_{xz}}{z_0 \varepsilon_{xx}} & 0 \\ 0 & 0 & 0 & -z_0 \\ 0 - \frac{\varepsilon_{yz}}{z_0} + \frac{\varepsilon_{xy} \varepsilon_{xz}}{z_0 \varepsilon_{xx}} & \frac{\beta \varepsilon_{xz}}{\varepsilon_{xx}} & \frac{\beta^2}{z_0} + \frac{\varepsilon_{xz}^2}{z_0 \varepsilon_{xx}} - \frac{\varepsilon_{zz}}{z_0} & 0 \end{pmatrix}, \tag{1.25}$$

which lets Snell's law ($\beta = n \sin\theta$) and permittivity constants of the material be directly computed, yielding the majority of a thin film's parameters.

The final step of the Berreman calculus is to determine the physical thickness of each material layer using the phase matrix, $\hat{A}_d$.[7]

1.6 The Daniel K. Inouye Solar Telescope

The National Science Foundation's (NSF) Daniel K. Inouye Solar Telescope (DKIST) completed construction on the summit of Haleakalā, Maui, Hawai'i in late 2021. As the largest optical

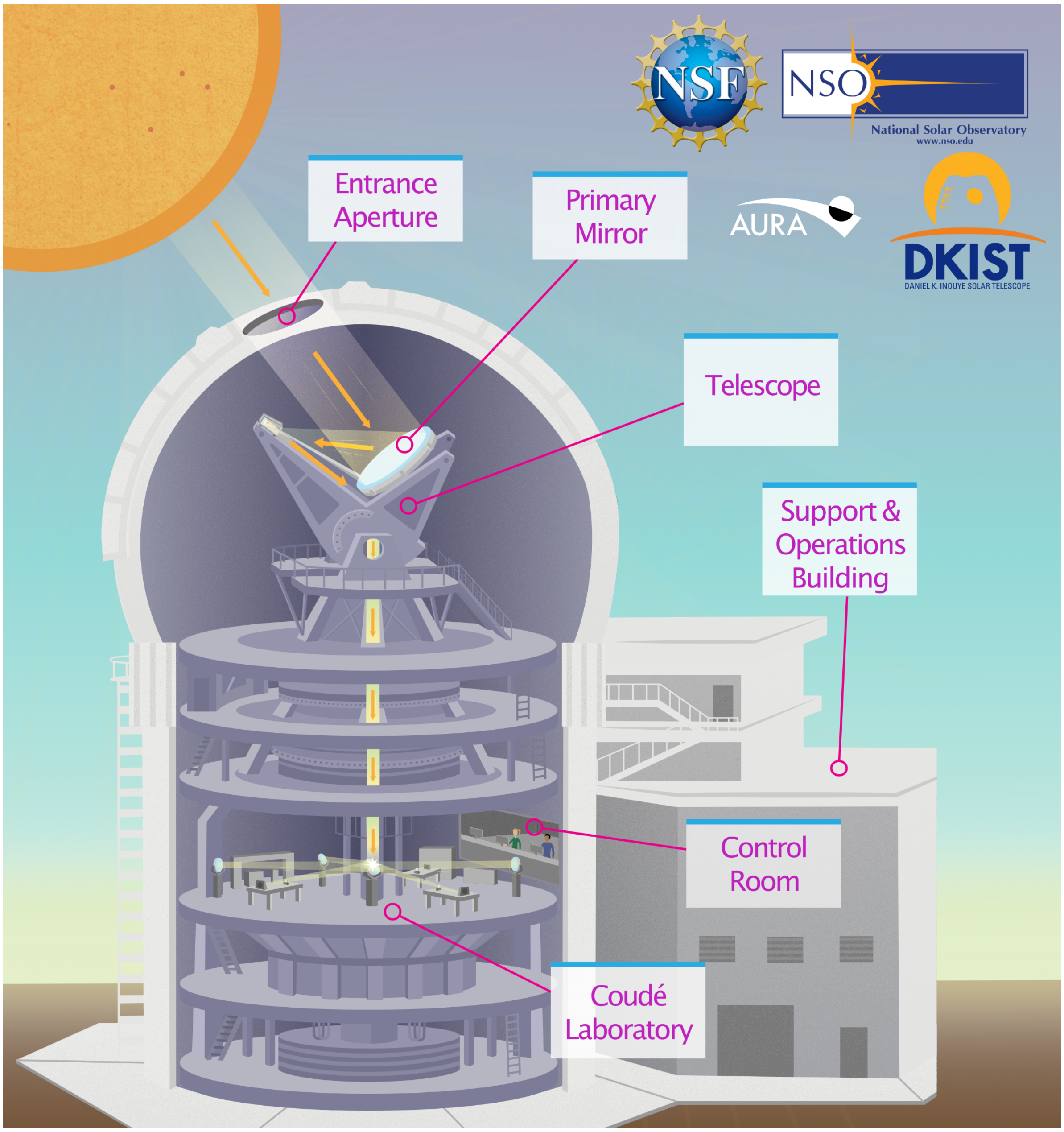

Figure 1.10: A cut-out drawing of the Daniel K. Inouye Solar Telescope (DKIST), a 4-meter, off-axis Gregorian solar telescope. DKIST observes the Sun with state-of-the-art imaging and spectroscopy instrumentation located in a rotating coudé laboratory. Diffraction-limited observations of the solar surface can resolve features as small as 20 km at a wavelength of 500 nm. *Adapted from nso.edu*

solar telescope in the world, DKIST is designed to provide high spatial-resolution spectroscopy and imaging over a spectral range of 380 nm - 5000 nm, in order to study the fundamental nature of the Sun's magnetic field. With a 4.2 m, off-axis, $f/2$ primary mirror (4.0 m illuminated) and a suite of spectropolarimetric and imaging instrumentation, DKIST delivers diffraction-limited resolution and sensitivity measurements of the Sun in order to study the origins of solar magnetism at a spatial resolution similar to modern magnetohydrodynamic (MHD) simulations.[24] Achieving a diffraction-limited resolution ($0.026''$ at 500 nm) is critical to many of the science questions DKIST seeks to answer, as is making reliable and well-calibrated polarimetry measurements.[24, 25] A full description of the DKIST observatory and its science goals can be found in the Observatory Overview and Critical Science Plan.[24, 26]

DKIST is an example of a complex, many-optic, articulated system. There are 11 facility mirrors that deliver sunlight to five first-light instruments and the wavefront correction system (Figure 1.10). The first six facility mirrors, M1 - M6, comprise a Gregorian telescope (M1 and M2) and the altitude (M3 and M4) and azimuth (M5 and M6) rotation axes. M6 relays the beam down to a climate controlled, instrument laboratory on a rotating coudé floor (Figure 1.11). M7 then levels the beam to be parallel with the floor followed by mirrors M8 and M9 collimating and positioning the beam. After M9, a small pick-off mirror, M9a, can be inserted into the beam, directing all observed wavelengths into the Cryogenic Near-Infrared Spectropolarimeter (Cryo-NIRSP).[27] Up until this point, DKIST's entire beam path is made up of reflective optics, allowing Cryo-NIRSP and any future instruments to observe at longer wavelengths than refractive optics allow. When M9a is not placed in the beam, light is relayed to the deformable mirror (DM or M10) used by the adaptive optics system. A corrected beam is then sent to the Facility Instrument Distribution Optics (FIDO), which is a light distribution system consisting of a series of dichroic beamsplitters and windows.[28] FIDO relays a split beam to the remaining instruments; the Visible Broadband Imager (VBI), the Visible Spectro-Polarimeter (ViSP), the Diffraction-Limited Near Infrared Spectro-Polarimeter (DL-NIRSP), and soon the, not yet installed, Visible Tunable Filter (VTF). Detailed descriptions of the four first-light instruments and telescope support facilities can

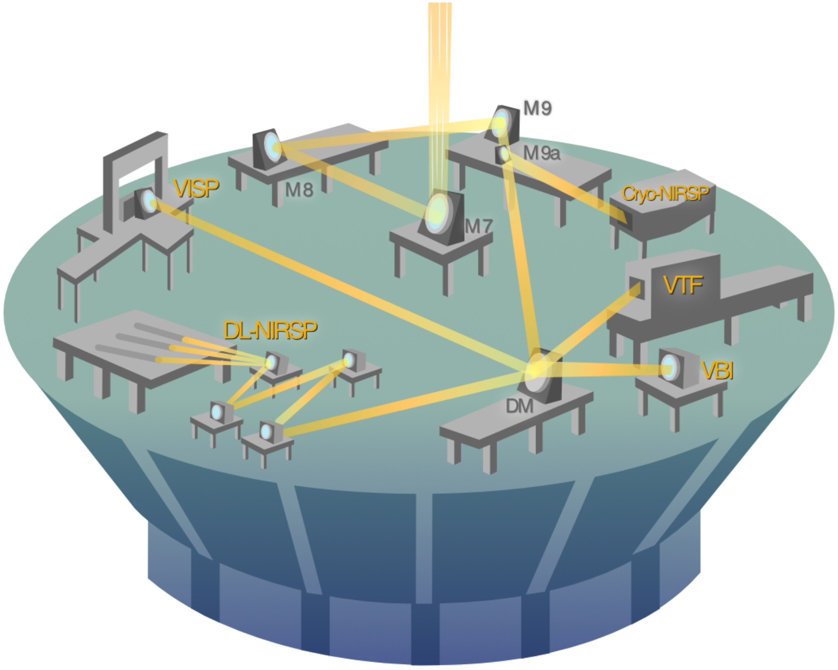

Figure 1.11: A rotating coudé floor houses mirrors M7 - M10 and DKIST's five first-light instruments: VBI, ViSP, DL-NIRSP, Cryo-NIRSP, and VTF. Light comes from the telescope above and is leveled and collimated by mirrors M7 - M9. M10 is the deformable mirror (DM) and is part of the adaptive optics (AO) system. From the DM, light is directed into FIDO to be dispersed to the four instruments which use AO. *Adapted from nso.edu*

be found in a special issue of *Solar Physics*.[25, 27, 29–32]

1.6.1 Polarization requirements

DKIST has been tasked with providing high-resolution, highly precise data to the solar community for the coming decades. The Sun is the most highly resolved star we can observe from Earth, and it provides us with a natural laboratory to study the fundamental properties of astrophysical plasmas. Understanding how small-scale structures of the Sun's magnetic field affect the physics of large-scale dynamics is a major science driver of DKIST. Other goals include gaining a better understanding of coronal-heating mechanisms and long-term dynamics of the solar cycle. Many science cases, including the ones above, have been laid out by the solar community in the Science Requirements Document and the Critical Science Plan.[26, 33] Most require some combination of high accuracy, high spectral resolving power, wide fields, and fast temporal cadences.

Many of the science questions DKIST will address rely on spectropolarimetric data. Science results are then only as accurate as the polarimetry measurements, constraining DKIST to very demanding polarimetry requirements – sensitivity levels to fractional polarization of 1×10^{-5} above background and an absolute error in the measured fractional polarization of 5×10^{-4}.[24,33] To achieve accurate polarimetric measurements, all potential errors must be mitigated or calibrated to levels below the required error threshold. Thus, DKIST has undergone multiple calibration campaigns in order to understand and minimize the causes of polarization error by creating a full polarization system model.[12,13,25,28,34–39]

1.6.2 Current DKIST Polarization Calibration System Model

The current polarization calibration system model for DKIST can be found in Harrington et al. (2023).[25] It provides a polarization model for the entire wavelength bandpass, 380 nm to 5000 nm, covered by DKIST as well as all combinations of azimuth-elevation-coudé table angle pointings. The model consists of a sequence of polarization calibrations done at different pointings combined with a database of mirror polarization responses to derive a modulation matrix. A modulation matrix is an $n \times 4$ transfer matrix with entries of the four components of the Stokes vector from the n modulation states. For DKIST, the modulation matrix includes everything on the coudé floor from mirror M7 to the instrument. The modulation matrix is multiplied by an incoming Stokes vector to obtain a column vector of the measured intensities, $\mathbf{I}_{\text{measured}}$.[25,39] This modulation matrix was then used as a representation of an optimal system modulation matrix, $\mathbf{O}_{\text{true}}$, yielding:

$$\mathbf{I}_{\text{measured}} = \mathbf{O}_{\text{true}} \mathbf{S}_{\text{true}}. \tag{1.26}$$

The Stokes vector that was measured, $\mathbf{S}_{\text{measured}}$, during the calibration sequence is then the product of a demodulation matrix, $\mathbf{D}_{\text{fit}}$ that has been fit for using a characterization of telescope optics, and the measured intensities:

$$\mathbf{S}_{\text{measured}} = \mathbf{D}_{\text{fit}}\mathbf{I}_{\text{measured}}. \tag{1.27}$$

Assuming the system errors are represented by the difference between the measured Stokes vector and the true Stokes vector, the error matrix, ϵ_{ij}, can be derived as:

$$\begin{aligned}
\Delta\mathbf{S} &= \mathbf{S}_{\text{measured}} - \mathbf{S}_{\text{true}} \\
&= \mathbf{D}_{\text{fit}}\mathbf{I}_{\text{measured}} - \mathbf{S}_{\text{true}} \\
&= \mathbf{D}_{\text{fit}}\mathbf{O}_{\text{true}}\mathbf{S}_{\text{true}} - \mathbf{S}_{\text{true}} \\
&= (\mathbf{D}_{\text{fit}}\mathbf{O}_{\text{true}} - \mathbf{1}_{\text{ij}})\mathbf{S}_{\text{true}} \\
&= \epsilon_{ij}\mathbf{S}_{\text{true}}
\end{aligned}$$

where $\mathbf{1}_{ij}$ is the identity matrix.

$$\therefore\ \ \epsilon_{ij} = \mathbf{D}_{\text{fit}}\mathbf{O}_{\text{true}} - \mathbf{1}_{\text{ij}} \tag{1.28}$$

Using this concept and a similar approach as that used on *Hinode*,[40] DKIST has specified its error matrix as:

$$\epsilon_{ij} = \begin{pmatrix} 10^{-2} & 10^{-2} & 10^{-2} & 10^{-2} \\ 5\times10^{-4} & 10^{-2} & 5\times10^{-3} & 5\times10^{-3} \\ 5\times10^{-4} & 5\times10^{-3} & 10^{-2} & 5\times10^{-3} \\ 5\times10^{-4} & 5\times10^{-3} & 5\times10^{-3} & 10^{-2} \end{pmatrix}. \tag{1.29}$$

Each element in the error matrix corresponds to an element of a Mueller matrix and represents the maximum uncertainty for that element. We can read this as a tolerance of 1% uncertainty in depolarization from the diagonal and II, QI, UI, VI terms (top row), 0.05% uncertainty in polarizance (first column), and a tolerance of 0.5% in the off-diagonal rotational terms.

1.6.3 Motivation: What DKIST (and others) left out

Polarization allows physical properties, such as the magnetic field strength, of an object to be inferred from observations without in situ measurements. Instrument performance predictions are, however, generally limited to predicting system polarization as functions of field of view, wavelength, and configuration.[12]

We note that this DKIST model, in addition to every other telescope model that we are aware of, does not include mirror depolarization in the system model. We aim to show here an upper limit to the error caused by ignoring depolarization caused by mirror-coating nonuniformity.

Chapter 2

Modeling the Polarization Behavior of Dielectric Mirror Coatings

This chapter is adapted from a proceeding paper[41] presented at the SPIE Astronomical Telescopes + Instrumentation 2022 meeting. A manuscript is being prepared for submission to JATIS.

System-level modeling of polarization performance at large astronomical telescopes has lagged behind other fields like adaptive optics and interferometry and must be addressed as science requirements of new facilities drive stringent limits on polarization accuracy. This is especially true for powered optics with a large variation of incidence angles across an aperture.[12] A powered optic is any optic that causes the outgoing beam to converge or diverge, hence changing the optical power. In the case of DKIST, there are four powered mirrors in the main telescope: M1, M2, M4 and M8. To accurately model mirrors and the induced system polarization, a coating model *specific to each individual optic* is required. This can be difficult to achieve, as coating formulas are often proprietary and variability in the deposition conditions can have large effects on coating behavior. Using standard coating formulas designed for reflectivity optimization may not be optimized for diattenuation and retardance as well, which are more important for polarization performance calculations to match than overall reflectivity.[12,13] As shown below, when the retardance and diattenuation of each individual mirror in a system are fitted for and the effective refractive index of the surface is modeled from basic physics, a more accurate determination of system performance can be made.

2.1 Measuring mirror samples

In order to model a realistic system, we must first have a realistic understanding of each component of the system individually. To achieve this, witness samples from all optical surfaces on DKIST that contribute to the modulation matrix described in Section 1.6.2 were measured with a Mueller matrix spectropolarimeter. A witness sample is a small optic that was present in the coating chamber when another optic of interest was being coated. Because they are small (usually 1"-2" in diameter), witness samples are easy to test and characterize compared to a large 0.5+ m optic. Samples spread around the coating chamber can also be used as a test of coating uniformity. The list of measured optics includes all ten facility mirrors, the calibration optics located at the Gregorian focus, all windows and beam splitters that make up FIDO, and steering mirrors for the instruments. This chapter will focus solely on mirrors; however, the details for all optics can be found in a series of papers titled *Polarization modeling and predictions for Daniel K. Inouye Solar Telescope*, Parts 1-9.[12,13,28,34–39]

2.2 Applying Berreman models fits to NSO Laboratory Spectropolarimeter Data

The majority of the data presented in this chapter has been obtained with the NSO Laboratory Spectropolarimeter (NLSP; Figure 2.2), a custom-built benchtop polarimeter used for metrology measurements of polarization optics. NLSP measures the Mueller matrix of a sample with a polarization state generator followed by a full Stokes polarimeter. The polarization state generator consists of a fiber-coupled, collimated light source that provides a circular beam to a rotating wire grid polarizer and a rotating crystal, third-wave, linear retarder. The calibration polarizer and calibration retarder rotate against each other through a series of nine orientations. This allows the generation of different polarization states to be sent to the sample. A rotating stage holding the sample to be measured follows the state generator in the beam path. Depending on the experimental setup, light is then sent to either the transmissive or reflective arm of NLSP. The transmissive

Figure 2.1: An example of a witness samples from the DL-NIRSP instrument. Witness samples are small optics that were present in the coating chamber when another optic of interest was being coated. The left image shows these samples as they arrived in the lab. Each is labeled with the name of the optic witnessed (mirrors 1, 1A, and 1B in DL-NIRSP) and an identifying coating run number. The right image shows witness sample DL-NIRSP-16BE16 mounted and ready for testing.

arm extends laterally from the sample, whereas the reflective arm of NLSP is positioned perpendicular to both the light source and the transmissive arm. Currently, the reflective arm can only be used at an angle of incidence of 45° on the sample.

Light then enters a rotating crystal, third-wave, linear modulator followed by a fixed analyzer. The modulator rotates once for each complete sequence of generated polarization states. It steps through six angles for a total of 54 measurements. The analyzer is a wire grid polarizer that doubles as a beam splitter, directing the beam through a set of fibers into both a visible and near-infrared spectrograph. The visible spectrograph covers a wavelength range of 380 nm − 1200 nm, while the infrared spectrograph covers wavelengths of 900 nm − 1650 nm. Although there are separate sets of nearly identical optics for each, both the transmissive and reflective arms of NLSP use the same set of spectrographs as detectors.

From NLSP data, a coating formula prescription for the optic is fit. The data are reduced in Mathematica to obtain an observed Mueller matrix, which is then fit with the Berreman calculus as described in Section 1.5, using a Python package transcribed from the MATLAB package outlined in McCall et al. (2015).[7] Our previous work achieved fitting of the data through a brute-force parameter search. Harrington et al. (2019)[13] used a grid search of common coating materials and thicknesses to fit the retardance of DKIST witness samples. The mirror to be fit is assumed to have two layers of dielectric over a silver metal layer and to be suspended in air (e.g. the glass substrate is ignored). Properties of dielectrics and silver metal are determined using publicly available refractive index data from individual sources found on the website `RefractiveIndex.INFO`.[42]

Following Equations 1.17 - 1.25, Berreman models for many different thicknesses of different materials were calculated systematically to obtain the theoretical reflected and transmitted Mueller matrices of many different coatings at all wavelengths in the NLSP bandpass. The retardance of each model was then calculated using Equation 1.13 and compared to the experimental retardance obtained from the measurements of the witness sample. The fit error is found by differencing the two curves as $\texttt{err} = \langle |R_{Berreman} - R_{NLSP}| \rangle$, and using the smallest residual as the best fit model.

Unsurprisingly, the fits obtained by Harrington et al. (2019)[13] matched the NLSP measure-

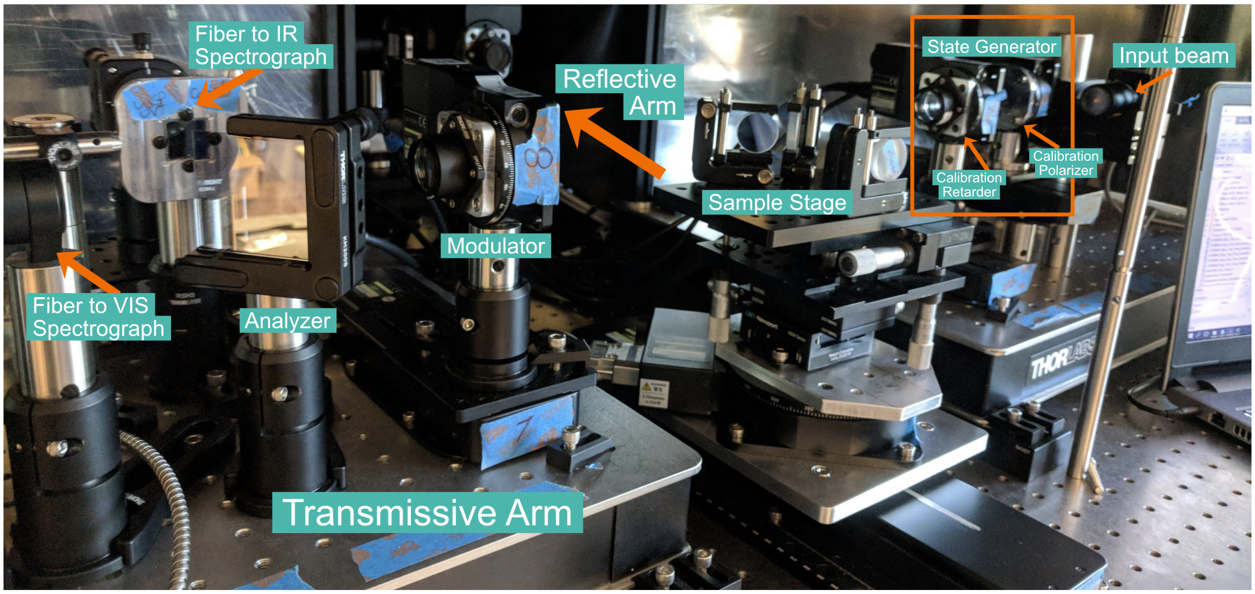

Figure 2.2: The NSO Laboratory SpectroPolarimeter, NLSP, is a benchtop polarimeter that has been used to take metrology measurements of DKIST coating samples. A collimated beam of white light is fed into the polarimeter on the right-side of the image. The beam then passes through a polarization state generator which consists of a rotating calibration polarizer and a rotating calibration retarder. The polarizer and retarder rotate incrementally against each other to generate different input Stokes vectors. The beam then either reflects or refracts off of a sample and it sent into the modulator. The modulator is another rotating retarder that steps through a series of rotation angles for each set of generated Stokes vectors. After being modulated, the beam is split by the analyzer, a fixed wire grid polarizer at 45°, into the visible and infrared spectrographs. The spectrographs run simultaneously and span a combined wavelength range of 380 nm – 1650 nm.

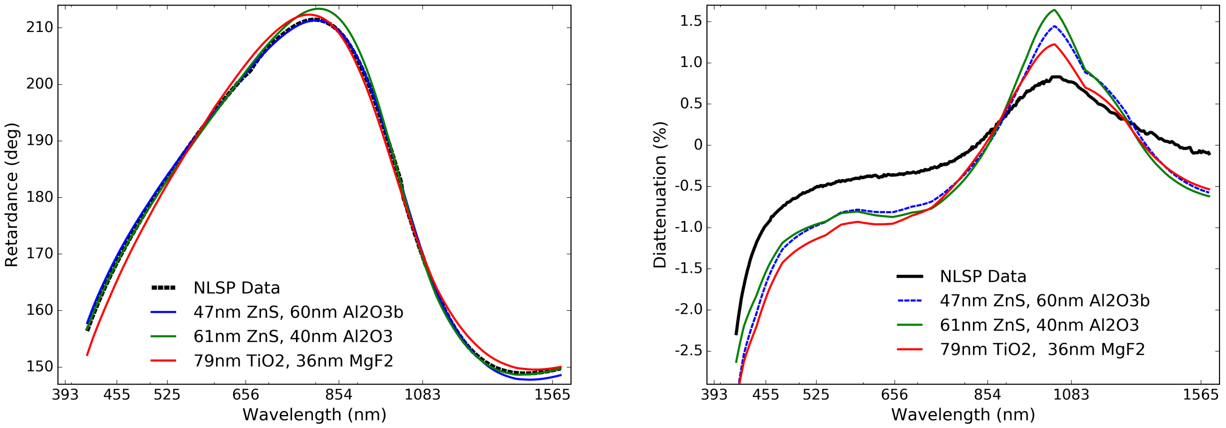

Figure 2.3: NLSP measurements and corresponding Berreman model fits. Left panel shows retardance fits to an enhanced protected silver mirror used at the GREGOR solar telescope along with some model fits using common coating formulas - Zinc Sulfide (ZnS) over Aluminum Oxide (Al_2O_3) and Titanium Oxide (TiO_2) of Magnesium Flouride (MgF_2). Right panel shows diattenuation measured with NLSP along with diattenuation predictions for the retardance-fit Berreman models. Retardance-fit only models do a very poor job of reproducing the observed diattenuation. *Reproduced from Figure 18 of Harrington et al. (2019).*[13]
Note: the "b" following Al_2O_3 *in the blue curve's label refers to the refractive index equation derived by Boidin et al.*[43]

ments fairly well and are reproduced here on the left side of Figure 2.3. However, by overplotting the modeled diattenuation predictions from the fits onto the observed NLSP data, as shown on the right side of Figure 2.3, it becomes fairly obvious that a retardance only model is not sufficient to fully reproduce observations from witness samples. Given that diattenuation is predominantly expressed by the QI and IQ terms and retardance is generally coded into the terms of the lower 3×3 matrix within the Mueller Matrix (see Equation 1.11), much of the information provided by the Mueller matrix is not accounted for unless both retardance and diattenuation are simultaneously constrained.

2.2.1 Optimizing for diattenuation

This chapter expands on Harrington et al. (2019)[13] by adding diattenuation to all model fits and also optimizing the code to expand its capabilities. The previous brute-force grid search used only two parameters to find the best-fit retardance: the thickness of layer 1 and the thickness of layer 2. Although simple to run, there is not much room to add complexity to the brute-force model without also exponentially increasing computational time.

The `differential_evolution()` algorithm from Python's `scipy.optimize` package was chosen for our code optimization. Differential Evolution[44] is a minimization method designed to find the global minimum of a given problem by stochastically sampling the solution while still utilizing a direct search method. By stochastically selecting areas to test, Differential Evolution is able to handle non-differentiable functions unlike the gradient-based searches of many other optimizers, and it is able to avoid falling into local minima. Other benefits of Differential Evolution include its easy implementation for any number of parameters, its presence as a standard algorithm in `scipy.optimize`, and it is quick to convergence compared to other optimizers.[44,45]

For retardance-only fits, Differential Evolution significantly reduced the computation time to fit a two-layer coating formula to the NLSP data. Run-times dropped to approximately 15 minutes from 24 hours, and the optimizer reproduced the results of our previously run brute-force searches. Optimization also allowed for increased complexity. A new error metric was introduced to account

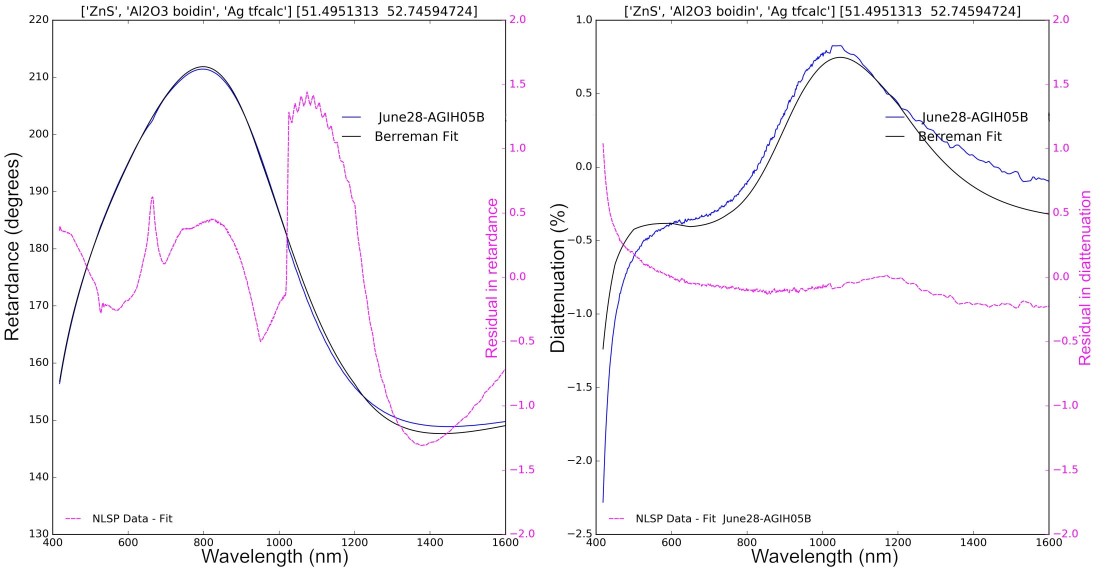

Figure 2.4: First model fit including diattenuation for an enhanced silver mirror used at the GREGOR solar telescope. The black model curves use the same formulas for dielectric layers as the blue curves in Figure 2.3. Overall, the addition of diattenuation has resulted in a significantly better fit to the data, with a slight deviation in retardance at long wavelengths.

for both retardance and diattenuation in the model fits. The expression now minimized by the Differential Evvolution fitter is of the form:

$$\texttt{err} = \langle |R_{Berreman} - R_{NLSP}| \rangle + \langle |D_{Berreman} - D_{NLSP}| \rangle \tag{2.1}$$

where retardance (R) is still calculated with Equation 1.13 and diattenuation (D) is given by $D = QI/II \times 100\%$. Here, the QI term of the Mueller matrix has been normalized by the II intensity element in order to remove the influence of transmission effects.

Adding diattenuation to our model fits resulted in a significant improvement in replicating the observed diattenuation data and slightly worse fit to retardance in the infrared. A newly optimized retardance + diattenuation model is shown in Figure 2.4. It was run on the same data set presented in Figure 2.3 and assumes a coating formula of ZnS over Al_2O_3, which correlates to the blue curves in Figure 2.3. The data curves are identical in both figures. In Figure 2.4, the black curves represent the fit of the model to NLSP data of a mirror witness sample on loan from the

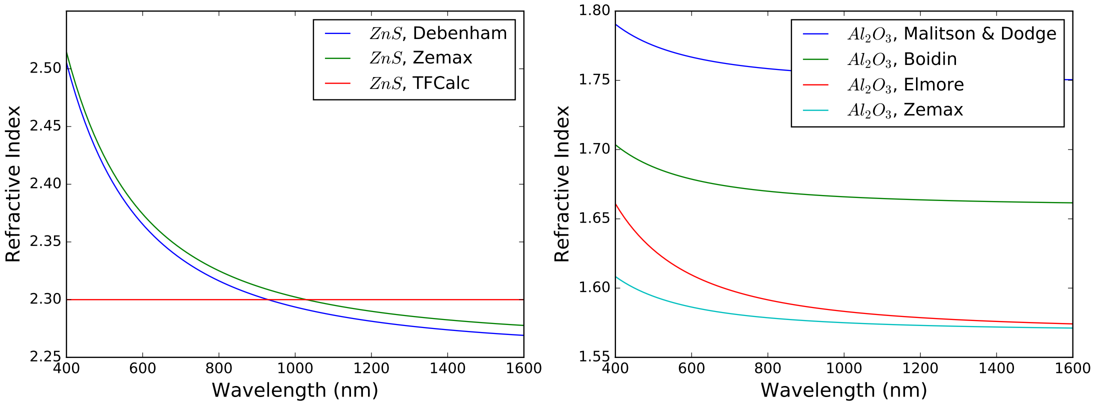

Figure 2.5: Example refractive indices for ZnS and Al_2O_3, two common dielectrics used in mirror coatings. Publicly available indices for a given material vary widely depending on the source and measurement method, as shown here. The authors of each measurement are listed in the legend labels of each curve.[43,46–49]

GREGOR telescope. The pink curves are the residual difference 'Data - Fit.' The retardance fit has remained about the same and is consistent with the data at most wavelengths; it is a slightly worse fit in the infrared with a 1° residual. The diattenuation fit, however, improved significantly and now follows the shape of the data. The predicted thicknesses of each dielectric layer also changed slightly, with values changing from 47 nm of ZnS over 60 nm of Al_2O_3 to 51.5 nm of ZnS over 52.7 nm of Al_2O_3. This represents a 2.8 nm change to the total dielectric thickness, and will be discussed in further detail in Section 2.3.

2.3 Refractive Index Concerns

In our previous work,[12,13,37,41] the refractive index of each dielectric layer was obtained from publicly available data. This became problematic for several reasons: refractive index data varies widely, even for the same material, depending upon factors such as the source of the data (e.g. how many wavelengths were measured, what technique was used), the material structure (e.g. crystalline vs. amorphous), and the deposition method (see Section 1.4.1). An example of the variety of publicly available refractive index dispersion curves for zinc sulfide (ZnS) and aluminum oxide (Al_2O_3) are shown in Figure 2.5. Some sources of data agree fairly well, such as

ZnS curves from Debenham (1984)[46] and the Zemax materials catalog (Figure 2.5, left panel; blue and green curves), while others report just one or two points and extrapolate for all wavelengths, as the Thin Film Calculator software (TFCalc)[47] has with its ZnS dispersion curve (Figure 2.5, left panel, red curve). For other materials, such as Al_2O_3, sources do not agree and a wide range of refractive indices have been published (Figure 2.5, right panel). However, all of the Al_2O_3 curves are situationally correct. Al_2O_3 has many forms ranging from precious gemstones in its crystalline form and ceramic insulators in its amorphous form. It is possible to find a material source that was measured under conditions similar to those of your coating of interest; however, doing so can be time consuming. With this in mind, it is much easier to fit an accurate refractive index for a particular coating sample.

These differences in refractive index data become more apparent in our Berreman-model fits. 64 models were run using different combinations of the ZnS, Al_2O_3, and Ag dispersion relations listed in Table 2.1. Figure 2.6 illustrates the results of these combinations. Each combination was fit to the same retardance and diattenuation data taken with NLSP of a GREGOR solar telescope mirror witness sample. Retardance fits remained roughly the same over all material combinations (left panel), with only a few degrees of difference between models. On the other hand, the diattenuation fits (right panel) varied widely, and only half of the material combinations coincided with the peak in the data at $\sim$1050 nm. Of the models that "matched" the peak, there is a wide spread of 0.4% diattenuation in the height of the peak, which is approximately 35% of the total peak. Furthermore, none of the material combinations reproduced the diattenuation behavior observed in the ultraviolet or near-infrared. From this plot, it is apparent that fits using a tabular index of refraction data would not provide accurate enough models for use in the DKIST polarization calibration. We would either need vendors to reveal their mirror formulas (and we thank Vendors 1 and 2 for providing their proprietary data for this work) or to generalize our fits further.

The plot of the thickness of the modeled ZnS layer versus the thickness of the modeled Al_2O_3 layer (Figure 2.7) reveals further differences caused by various combinations of refractive

ZnS	**Al_2O_3**	**Ag**
Debenham (1984)[46] †	Malitson & Dodge (1972)[48] †	McCall et al. (2015)[7] ††
TFCalc[47]	Boidin et al. (2016)[43] †	TFCalc[47]
Zemax	Elmore ‡	Vendor 1 ‡
$n_{ZnS_{shift}}$	Zemax	Vendor 2 ‡

Table 2.1: Sources of refractive index data that went into the 64 model combinations used to produce Figures 2.6 and 2.7. $n_{ZnS_{shift}}$ is the Debenham dispersion − 0.1 at every wavelength. †Data file obtained from refractiveindex.info;[42] ††Only plotted in Figure 2.7;
‡Private communication

indexes. There is an overall trend for the total thickness of the dielectric layers to be constant (μ = 106.34 nm ± 5.31 nm) with large variations in the thickness of any given layer. A lower refractive index in the first dielectric layer resulted in a thicker second Al_2O_3 layer but still an overall thickness for the two dielectric layers of ∼106 nm. This trend appears to hold for large changes in the refractive index. A hypothetical refractive index curve, $n_{ZnS_{shift}}$, was generated by subtracting 0.1 from the dispersion curve presented in Debenham (1984)[46] at all wavelengths to see how the total dielectric thickness would change. Models using $n_{ZnS_{shift}} = n_{ZnS} - 0.1$ are plotted as horizontally half-filled points, and form a line with a slope similar to that of other combinations, but with a constant total thickness of ∼111 nm.

Ignoring models that use the McCall et al.(2015)[7] refractive index formula for Ag (circular points), Figure 2.7 also indicates that the refractive index for the base metal contributes little to the thicknesses of the dielectric layers as models that use the same refractive indices for ZnS and Al_2O_3 but different Ag are clumped together. The Ag from McCall et al. is highly extrapolated in the infrared, which may contribute to those combinations appearing as outliers. It is more likely that the metallic layer is a driver of diattenuation; models which used the same Ag refractive index curves tended to peak at similar diattenuation levels in Figure 2.6.

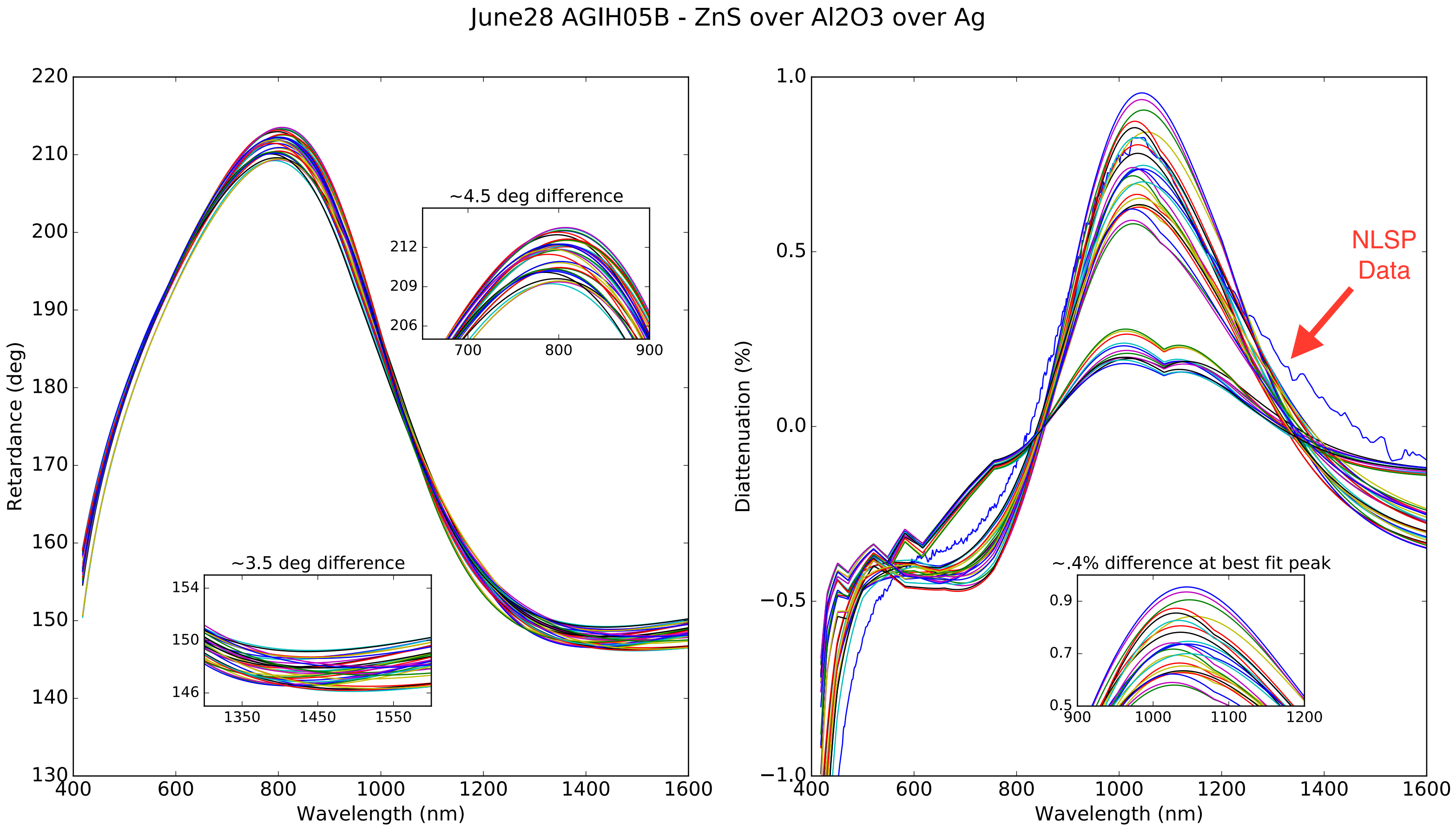

Figure 2.6: Plotted are the results of 48 different combinations of the ZnS, Al_2O_3, and Ag dispersion relations, listed in Table 2.1 Berreman models were fit to retardance and diattenuation measured with NLSP data from a GREGOR solar telescope mirror witness sample. Retardance fits remained roughly the same over all material combinations (left panel), with a few degrees of difference between models. Diattenuation fits (right panel) varied widely with only half of the material combinations matching the peak in the data at ~ 1050 nm.

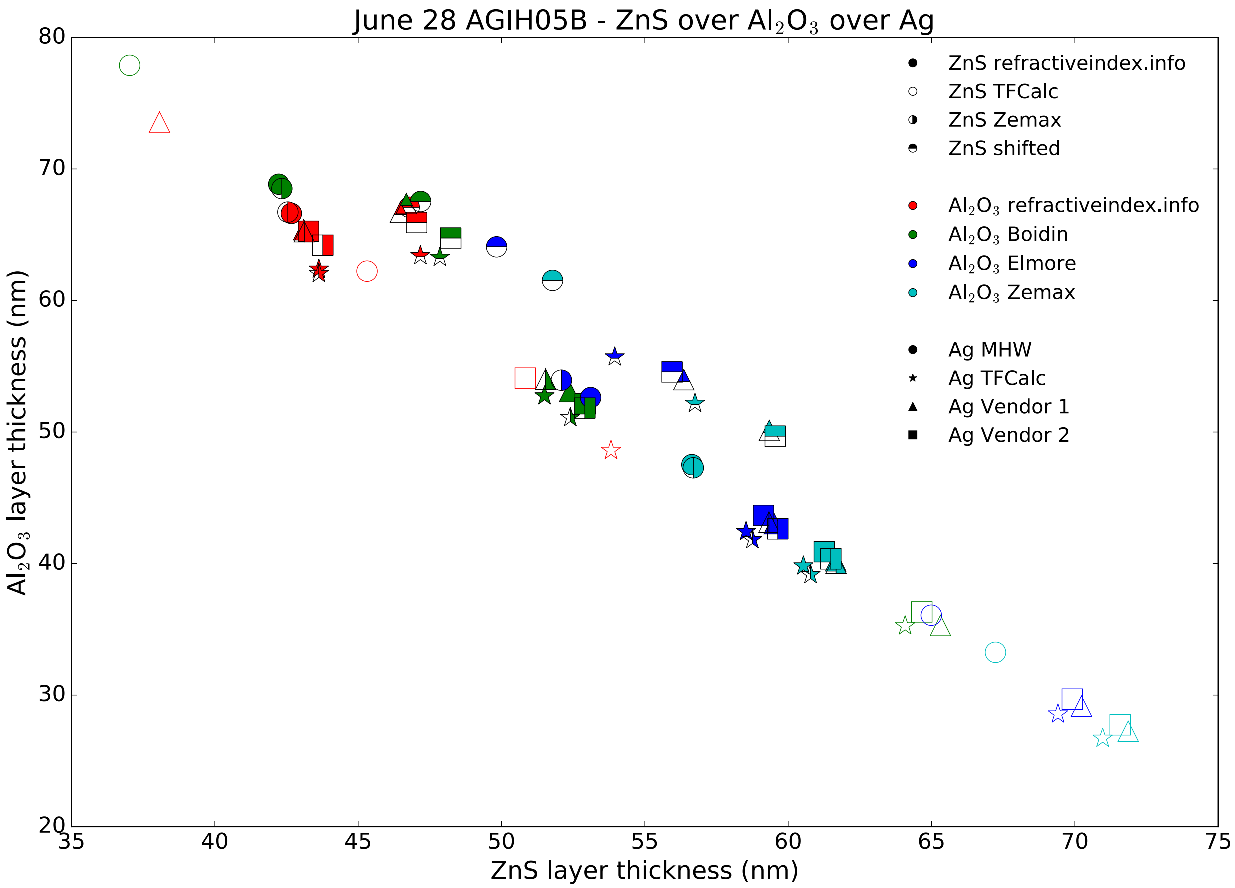

Figure 2.7: Modeled thickness of the ZnS layer versus the thickness of the modeled Al_2O_3 layer for the 64 combinations of materials listed in Table 2.1. There is an overall trend for the total thickness of the dielectric layers to be constant ($\mu = 106.34$ nm $\pm$ 5.31 nm) with big variations in the thickness of any given layer. Ignoring models which use the McCall et al.(2015)[7] refractive index formula for silver, there is evidence that the refractive index for the base metal contributes little to the thicknesses of the dielectric layers as models using the same ZnS and Al_2O_3 refractive indices are clumped together.

2.3.1 Cauchy Equations

Understanding how refractive index effects layer thickness, retardance, and diattenuation does not fully solve the problem of finding a appropriate dispersion curve to use when fitting coating data. To some degree, it doesn't really matter what the coating is (...for modeling an existing coating. What material used is still very important for coating design!) What matters is the effective refractive index of the optic being modeled at every wavelength. In order to generalize our fitting code, we have added the option of fitting a Cauchy equation to an unspecified material instead of relying on available refractive index data.

In 1836, Augustin-Louis Cauchy defined an empirical relationship between refractive index of a transparent material and the wavelength of light. The first successful empirical dispersion relation, Cauchy equations fit experimental data well, assuming the material has no optical absorption, at visible wavelengths with deviations in the ultraviolet and infrared regimes.[50] Even with these limitation, we opted to use a Cauchy equation in our fits due to the relations simplicity and ease of implementation, especially compared to other dispersion equations such as the Sellmeier equation.

Cauchy equations have the form:

$$n(\lambda) = B + \frac{C}{\lambda^2} + \frac{D}{\lambda^4} + ... \tag{2.2}$$

where λ is typically in μm and the coefficients take on values such that B > 1 > C > D.

We use a two term equation with coefficients B and C. The B coefficient is a dimensionless number that essentially sets the y-intercept of n. C has units of μm^2 and controls the curvature of the refractive index curve (See Figure 2.8). With the addition of Cauchy equations, the number of parameters in our models has tripled. Each dielectric layer is now fit for thickness, Cauchy B, and Cauchy C, bringing the total number of parameters used in fitting a two-layer mirror up to six. We have imposed several bounds on the Cauchy coefficients to force a physical solution. B values are permitted to range from $0-3$ while C values range from $0\ \mu\text{m}^2 - 1\ \mu\text{m}^2$. Additionally, the average value of the refractive index is required to satisfy $1 < \text{n}(\lambda) < 2.5$ to further insure physicality and

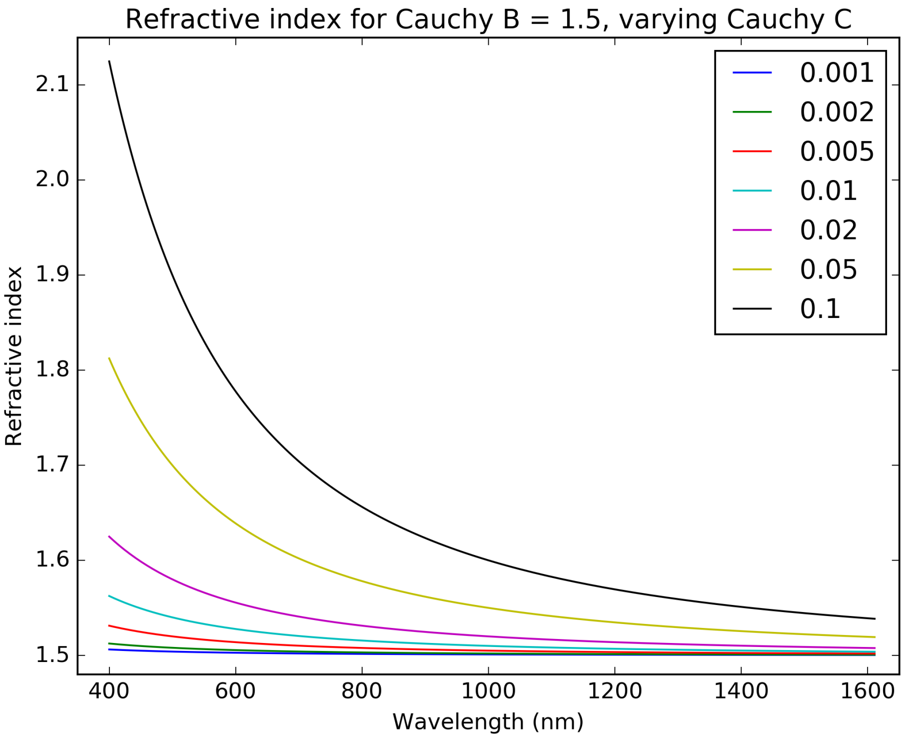

Figure 2.8: General refractive index curves for a two-term Cauchy equation with a constant B of 1.5 and varying C. The B coefficient sets the y-intercept of the Cauchy equation. The C coefficient controls the curvature of the dispersion curve, with higher C resulting in a larger change in refractive index between wavelengths.

to protect from singular matrices appearing in the characteristic matrix evaluation of the Berreman calculus.

2.3.1.1 Model sensitivity to Cauchy variables

As noted in Figure 2.8, the Cauchy C coefficient controls the shape and curvature of the refractive index curve. This influences both the retardance and diattenuation of a material as a shifting of the peak retardance and peak diattenuation as on the left side of Figure 2.9. For thicker layers of dielectric with multiple peaks of retardance, a high value of Cauchy C also affects the number of retardance and diattenuation peaks as well as their location. For example, in the right panel of Figure 2.9, a Cauchy C value of 0.1 μm^2 results in an additional third peak in retardance and a slight shift of the peaks to longer wavelength compared to the other values explored here, each of which has two peak retardance values. There is also a third peak in diattenuation for Cauchy C values of 0.05 μm^2 and 0.1 μm^2.

Similar behavior is observed when the Cauchy B coefficient is varied and the Cauchy C coefficient is held constant for a given layer thickness. Cauchy B is analogous to the y-intercept of a straight line and sets the lowest possible value of the refractive index when Cauchy C $= 0$. Using Snell's Law, as the refractive index of the dielectric layer increases with increasing B, the angle of refraction decreases. The speed at which light travels in the medium also slows. This leads to peak retardance and diattenuation values shifting to longer wavelengths. A large B values, the peak value of diattenuation also increases, there is almost a 3% difference between B $= 1$ and B $= 3$ as in Figure 2.10.

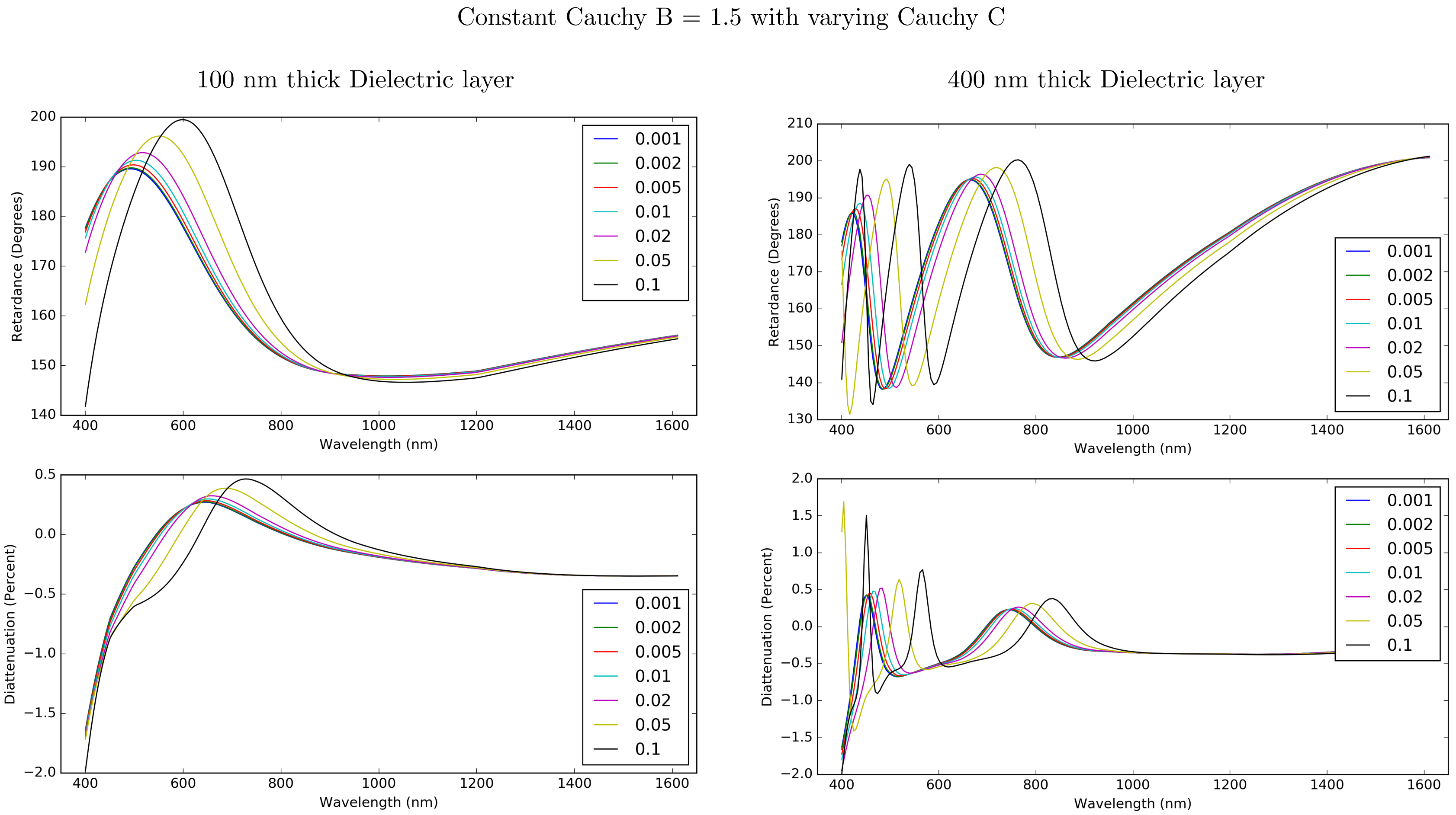

Figure 2.9: Example ranges of retardance and diattenuation curves for refractive index dispersion curves set with a constant Cauchy B coefficient and a range of Cauchy C values. A larger Cauchy C coefficient shifts both the peak retardance and peak diattenuation to longer wavelengths.

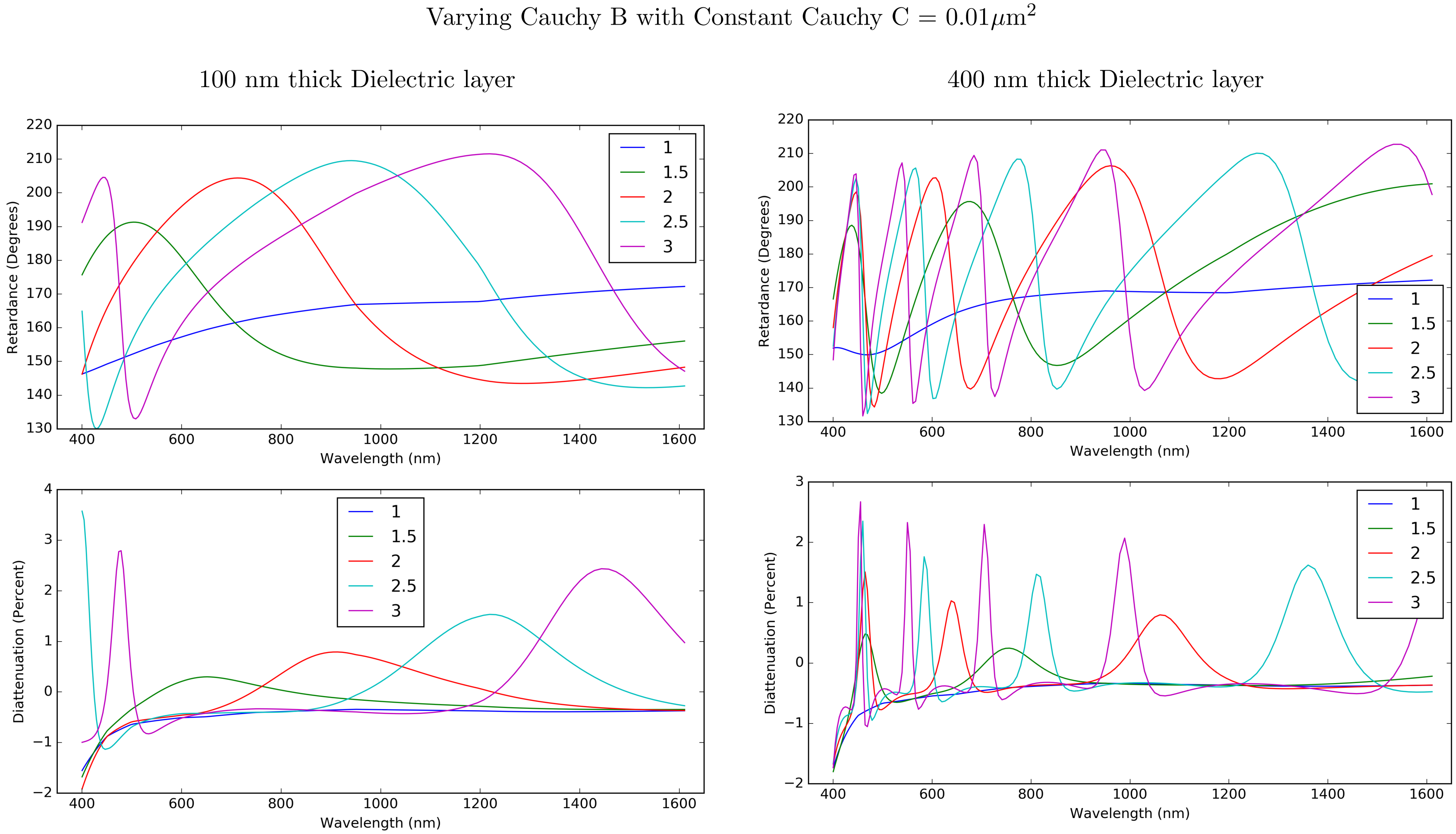

Figure 2.10: Example ranges of retardance and diattenuation curves for refractive index dispersion curves set with a constant Cauchy C coefficient and a range of Cauchy B values. A larger Cauchy B coefficient increases the overall refractive index of the material. Here we see a shift of peak values to longer wavelengths and increase in the peak values of diattenuation.

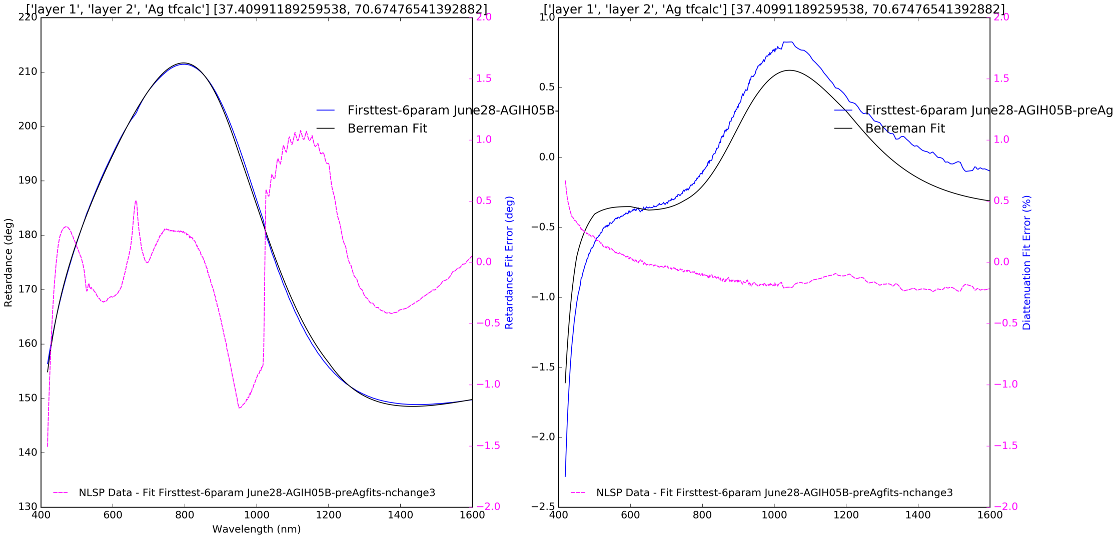

Figure 2.11: Berreman model fit with the addition of Cauchy equations for an enhanced silver mirror used at the GREGOR Solar Telescope. Compared to the tabular fit in Figure 2.4, retardance fit improved slightly in the infrared, however the diattenuation fit worsened near the 1050 nm peak.

2.4 Fitting Cauchy dispersions to NLSP data

With the addition of Cauchy fits, models of the GREGOR mirror sample slightly improved the retardance fit at infrared wavelengths, while the diattenuation fit degraded around 1050 nm (Figure 2.11). Looking at the fit refractive index curves for each of the two dielectric layers (Figure 2.12), results are mixed. The top layer was found to have a high refractive index, potentially a higher index than the ZnS guess used in previous analysis. This result is a little unexpected because the model fit indicates that the refractive index of the top dielectric is close to n = 2.9 at 400 nm which is not realistic. Silicon Carbide (SiC) exhibits one of the highest known refractive indices with n = 2.65 at 400 nm.[51] One possible explanation for this is that the coating actually contains three or more dielectric layers instead of the modeled two; the effective refractive index of multiple materials could be higher than the refractive index of any of the individual materials. Another possibility is a need to refine the boundaries of the Differential Evolution algorithm and reassess how a physical refractive index curve should be defined. Currently, the average n over all wavelengths is used to

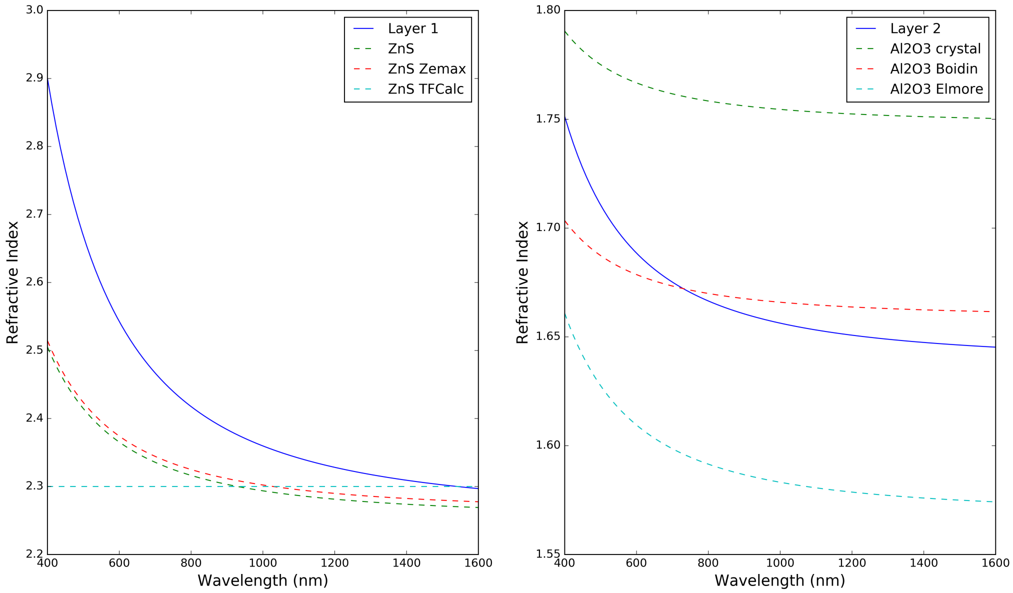

Figure 2.12: Refractive index curves obtained from Berreman model fit with the addition of Cauchy equations for an enhanced silver mirror used at the GREGOR Solar Telescope. The fits are plotted against select tabular refractive index dispersion curves seen in Figure 2.5. The Layer 1 refractive index is not physical for a single layer of material; the highest known natural refractive index at 400 nm is 2.65 for SiC. The Layer 2 dielectric agrees best with the Boidin[43] dispersion for amorphous Al_2O_3, falling between the other curves.

check the boundary conditions, but it may be more appropriate to set a maximum n value for short wavelengths. The fit of the second dielectric layer model is in good agreement with the public data for amorphous Al_2O_3, falling between the other curves and maintains an appropriate shape.

2.5 Single Layer Samples

To simplify our models, we obtained mirror samples of known single-layer dielectric coatings from Infinite Optics Inc (IOI) as well as purchased standard off-the-shelf, protected silver mirrors from ThorLabs and Edmund Optics with unknown proprietary coatings. The goal of acquiring these single-layer samples was to further explore our fits in a known parameter space to limit the number of parameters in an unknown sample. From IOI, we purchased a total of six 1-inch round samples of two different coating formulas: three are samples of the PAg1-350 which is SiO_2 over

PAg1-350		**PAg2-350**	
SiO_2	119 nm	Al_2O_3	341 nm
Ta_2O_5	2 nm	Ag	65 nm
Ag	180 nm	NiCr	15 nm
NiCr	15 nm	Glass Substrate	
Glass Substrate			

Table 2.2: Nominal formulas and layer thicknesses for the single-layer coating samples as provided by Infinite Optics

silver with two adhesion layers(tantalum pentoxide; Ta_2O_5, and nickel-chromium; NiCr), and three are samples of PAg2-350, the formula for which is Al_2O_3 over silver with a single nickel chromium adhesion layer. The nominal formulas and layer thicknesses supplied by IOI for these coatings are given in Table 2.2.

2.5.1 Ignoring Adhesion Layers

To explore the known parameter space, the first thing we looked at was the effect, if any, of the adhesion layers on the overall properties of a coating. Silver and in general most metals do not bond well directly to glass and consequently very few, if any, mirrors are actually a single layer of dielectric over metal.[17] A protective silver coating will often employ a thin nickel chromium (NiCr) adhesive layer between the metal layer and the glass substrate, as demonstrated by the formulas of the IOI samples listed in Table 2.2.

To limit the number of parameters used, it is much simpler to ignore any adhesive layers and model only the primary metal and dielectric layers. Using the Berreman calculus and the formulas provided by IOI, we assessed the impact of adhesion layers on the final retardance and diattenuation of our samples. Figure 2.13 shows the retardance and diattenuation of sample 9409-1, one of the IOI PAg2-350 samples, from reflective data obtained with NLSP. Also plotted are a Berreman forward model using the full IOI formula and a Berreman model that excludes the NiCr adhesion layer. We

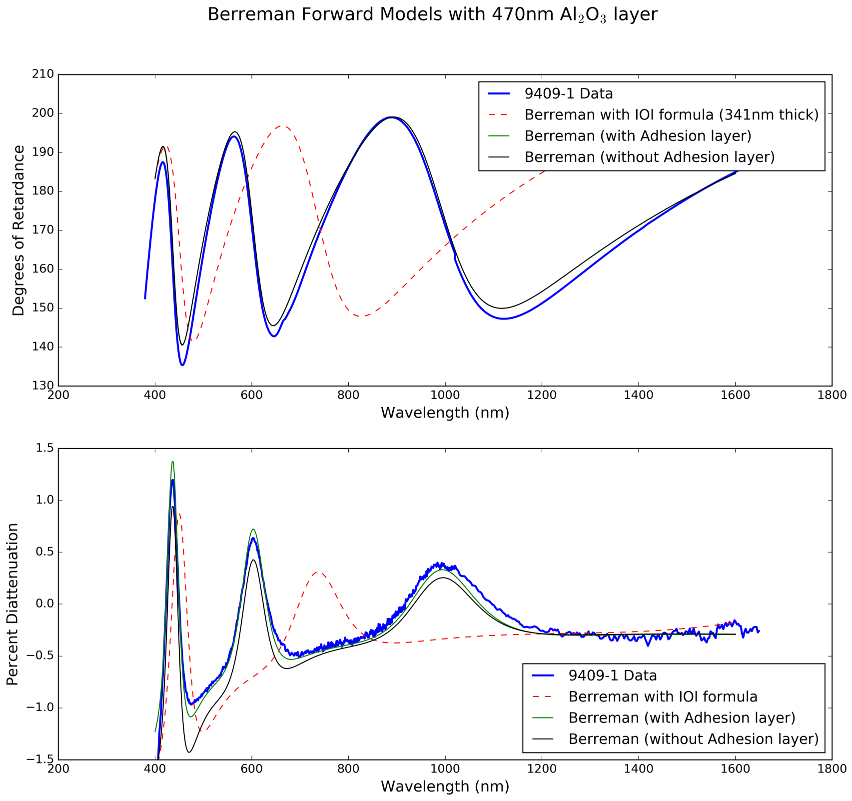

Figure 2.13: Forward Berreman models of a IOI PAg-2 sample with and without a NiCr adhesion layer are compared with data obtained with NLSP. These models were calculated using publicly available refractive index data for which the inital aluminum oxide layer thickness provided did not fit the data well (dotted line). Instead, we use a thicker 470 nm layer of Al_2O_3 and all other values listed in Table 2.2.

note that a thicker Al_2O_3 layer of 470 nm (black and green curves) was found to be a better fit to the data than the model using 341 nm IOI suggested (red, dotted curve). This difference could be due to our choice of refractive index data used or a number of other factors. We proceeded to use the 470 nm layer thickness of Al_2O_3 for the remainder of the analysis but kept all other thickness values consistent with the formula provided by IOI in Table 2.2.

Figure 2.14 shows the differences between the two models in the previous plot for both retardance and diattenuation. An adhesive layer of 15 nm NiCr between a glass substrate and silver coating results in $< 0.2°$ difference in retardance for wavelengths longer than 600 nm and $< 0.3\%$ difference in diattenuation compared to the model without the adhesion layer. The sys-

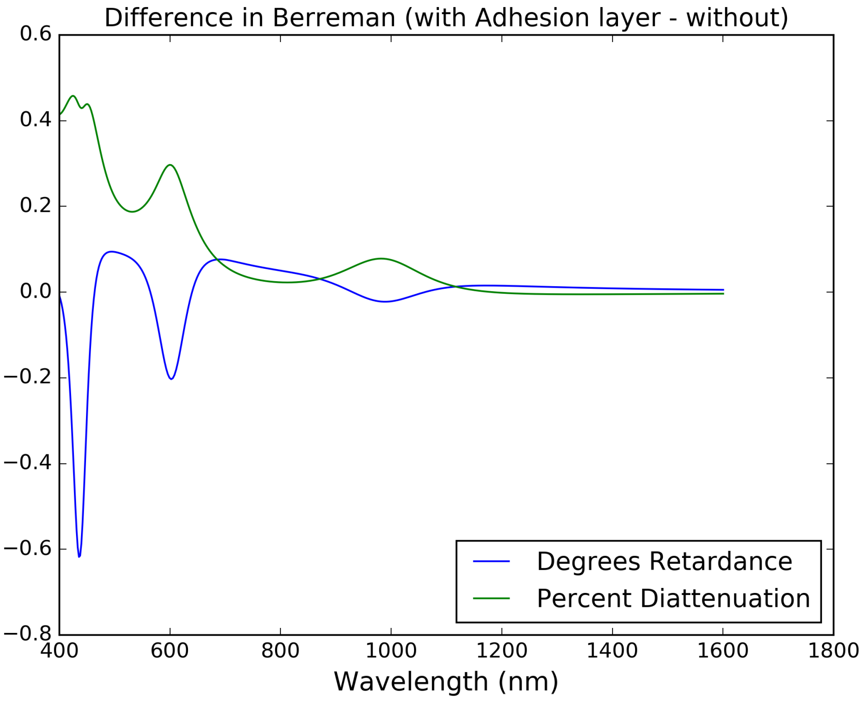

Figure 2.14: The difference between the retardance and diattenuation curves for Berreman models run with and without the presence of an adhesion layer. The systematic uncertainites in NLSP measurements are ∼0.2° retardance and at least of order ∼0.2% in diattenuation.[13] Excluding very blue wavelengths, these modeled differences are washed out by systematic errors and adhesion layers can be ignored.

tematic uncertainites in NLSP measurements are ∼ 0.2° retardance and at least of order ∼0.2% in diattenuation.[13] Excluding very blue wavelengths, these modeled differences are washed out by systematic errors. From this we conclude that we are able to ignore all adhesion layers and model mirror coatings as simply a single dielectric layer over a metal layer.

2.6 Summary

This chapter expanded on Berreman models from Harrington et al.[13] to create model fits of Mueller matrix data without the need for in-depth knowledge of the coating process that was used to manufacture an optic. An optimization module was added in order to avoid the long computation times required for brute-force searches. Optimization also allowed for expanding the parameter space searched to include a simultaneous fit to diattenuation in addition to the retardance space previously searched. Implementing a Cauchy equation fit has removed any reliance on the need for information on the material, layer thickness, or refractive index dispersion of a coating. We also showed that any sample can be treated as a single-layer dielectric, ignoring the adhesion and metal base layers. If the refractive index is free to be n $\geq$ 2.6, e.g., not a material found naturally, the effective refractive index of the sample is fit.

It is still unclear how best to balance the weighting of retardance and diattenuation errors when fitting for both. A cursory first-look has indicated that the two terms of the error metric (Equation 2.1) should not be weighted equally when minimizing. Retardance should have more weight than diattenuation, however the exact ratio of the two terms is not yet understood. Adding fits to the metal layers may help with this balance. We showed that the metal layer drives most of the diattenuation in Figure 2.6. Lookup table data is still being used in our models as the complex nature of metallic refractive indices complicates our fits. The imaginary part of a metallic refractive index can be easily fit with a straight line, adding two parameters to our model for the slope and y-intercept. However, we have not found a suitable polynomial to fit the real component. We attempted a three-parameter fit of a parabola in Figure 2.15 however were unable to obtain a suitable fit to either our data set or the general behavior seen in published dispersion formulas for silver. As a parabola fit to the real component represents five new parameters to our model, three for the real component and two for the imaginary, for a total of eleven in this version of the model, we are hesitant to go immediately to higher-order polynomials. This would be an interesting area for future work to tackle.

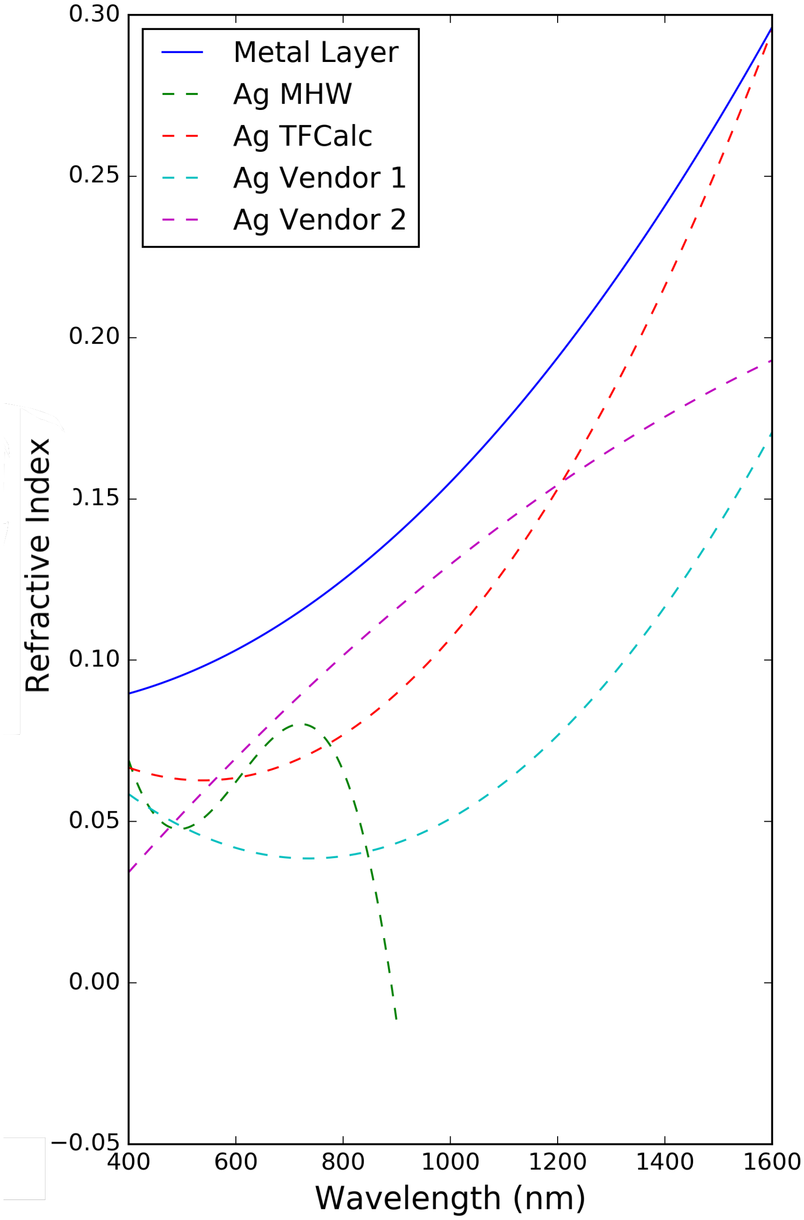

Figure 2.15: We attempted a three-parameter fit of a parabola to the real component of a metallic refractive index, however were unable to obtain a suitable fit to either our data set or the general behavior seen in published dispersion formulas for silver shown here. We have not found a suitable polynomial to fit and are hesitant to go to higher order polynomials.

Chapter 3

Loss of polarization due to coating non-uniformity

This chapter is adapted from a proceeding paper[52] presented at the SPIE Astronomical Telescopes + Instrumentation 2022 meeting. A manuscript containing Chapters 3 and 4 is being prepared for submission to JATIS.

In this chapter we explore how mirror coatings can decrease the incoming polarization signal and cause a loss through instrumental depolarization. As in the other chapters, we use the standard definitions of Stokes parameters ($\boldsymbol{S} = [I, Q, U, V]^T$) and Mueller matrices to describe polarization.[4]

Depolarization is a reduction of the Degree of Polarization (DoP) of polarized light. Any randomization of the average polarization over an aperture is depolarization. DoP is defined as:

$$DoP(\mathbf{S}) = \frac{\sqrt{S_1^2 + S_2^2 + S_3^2}}{S_0}, 0 \leq DoP \leq 1 \tag{3.1}$$

where S is the incoming Stokes vector. A DoP of 1 indicates that the light is fully polarized, likewise, a DoP of 0 is unpolarized light, and anything in between is partially polarized.

In the following analysis, we use two single number metrics to infer the degree of depolarization occurring to an incoming polarized beam. While these metrics do not fully represent the nine degrees of freedom representing depolarization in a Mueller matrix, these single number metrics give insight into polarization behavior with simple calculations. The depolarization index, (DI),[4, 53–55] represents the deviation of a normalized Mueller matrix from an ideal depolarizer and is defined as

$$DI(\mathbf{M}) = \frac{\sqrt{\left(\sum_{i,j} M_{ij}^2\right) - M_{00}^2}}{\sqrt{3}M_{00}}. \tag{3.2}$$

The second metric we use to quantify depolarization is the Average Degree of Polarization:[4]

$$AvgDoP(\mathbf{M}) = \frac{\int\limits_{0}^{\pi} \int\limits_{-\pi/2}^{\pi/2} DoP(\mathbf{M} \cdot \mathbf{S}(\theta, \eta)) \cos{(\eta)} d\eta d\theta}{2\pi} \tag{3.3}$$

which is the mean degree of polarization of exiting light averaged over all possible input states. Similar to the DoP, when the average DoP equals 1, the exiting light is completely polarized. When the average DoP equals 0, the exiting light is completely unpolarized, and the optic interacted with is a full depolarizer.

3.1 Code Validation

A code was written to simulate a flat mirror aperture with nonuniform coating in different configurations. The code assesses depolarization at each location on the aperture and over the average aperture. Its results were validated against example problems from the textbook *Polarized Light and Optical Systems*.[4]

3.1.1 Summing Linear Polarizers

Example 6.9 in *Polarized Light and Optical Systems* considers two linear polarizers with a fraction of the aperture (α) covered by a Horizontal Linear Polarizer (HLP) and the remaining fraction ($1 - \alpha$) covered by a Vertical Linear Polarizer (VLP). Using the example problem as a benchmark, our code can reproduce the expected mathematical result of an average DoP = 0.499 and a DI = 0.579 at $\alpha = 50$ as well as the accompanying Figures 6.21 and 6.22.[4] Our reproduction of those figures is shown here in Figure 3.1.

By changing the VLP to a linear polarizer at 45°(LP45), we have also reproduced *Polarized Light and Optical Systems* Figure 6.23 degree of polarization map for summing an HLP and LP45

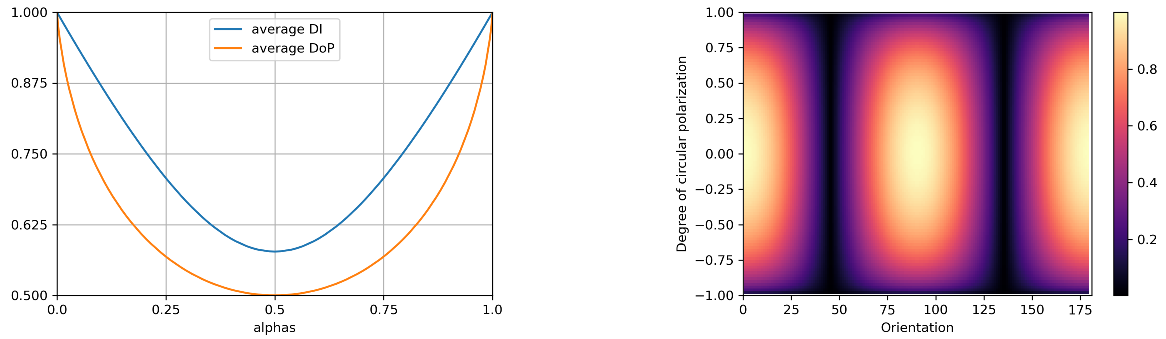

Figure 3.1: Our code successfully reproduces the DI and the average DoP for a HLP and a VLP covering an aperture as well as the DoP surface on the Poincaré sphere. The left shows DI and DoP averaged across an aperture that is covered by different fractions of HLP and VLP. The right figure reproduces the Poincaré surface for a HLP and VLP each covering 50% of an aperture. These are being compared to Figures 6.21 and 6.22 in the textbook *Polarized Light and Optical Systems*.[4]

over an aperture as shown here in Figure 3.2. With these reproductions, we are confident in the results our code produced for retarders and protected silver coatings in the following sections.

3.1.2 Exploring the behavior of Retarders

Building off of the text book examples, we also explored the behavior of a pair of ideal quarter wave linear retarders (QWLR) and found a similar behavior to the polarizers (left side of Figure 3.3). For a horizontal retarder (HQWLR, 0°) summed with a vertical retarder (VQWLR, 90°), the average DI over the aperture followed an identical behavior as the average DI of the polarizers (Figure 3.4). The average DoP over the aperture dropped with a much steeper overall slope than that of the polarizers while still bottoming out at an average DoP of 0.5. We can better visualize this with a DoP surface plot as on the right side of Figure 3.3. The contours on a DoP surface plot show the magnitude of depolarization for different incident polarization states.[56] Orientation of the linear polarization, a combination of Stokes Q and U, is shown on the x-axis. The y-axis shows the degree of incoming circular polarization. For this pair of retarders, the highest magnitude of surface DoP occurs at linear polarization orientations of 0° and 90° where Stokes Q = 1. Additionally, there is no surface polarization in the orthogonal state at orientations of 45° and 135°; i.e. Stokes

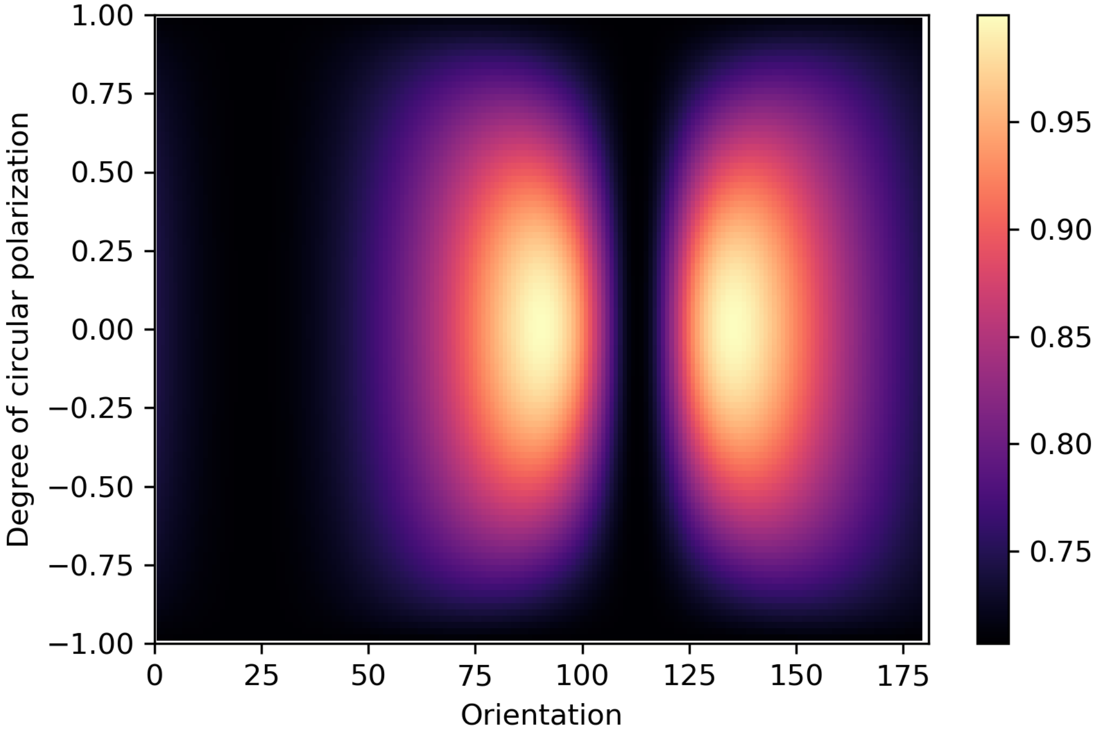

Figure 3.2: Our code successfully reproduces the DI and the average DoP map for a HLP and a LP at 45° covering an aperture as compared to Figure 6.23 in the textbook *Polarized Light and Optical Systems*.[4]

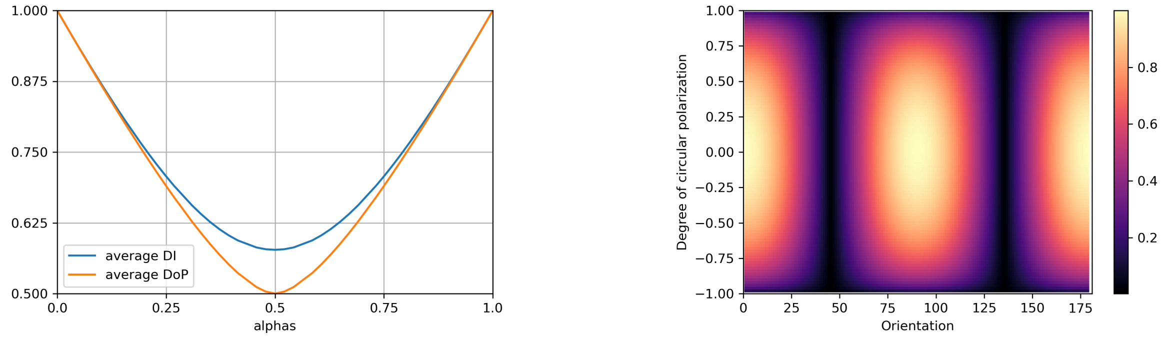

Figure 3.3: Shown here is the result of repeating Exercise 6.9 in *Polarized Light and Optical Systems*[4] with a HQWLR and a VQWLR summed over the aperture rather than a pair of polarizers. In the left plot, the average DI remains the same as the polarizers, however, the average DoP of the set of retarders decreases with a much steeper overall slope than the average DoP of the set of polarizers.

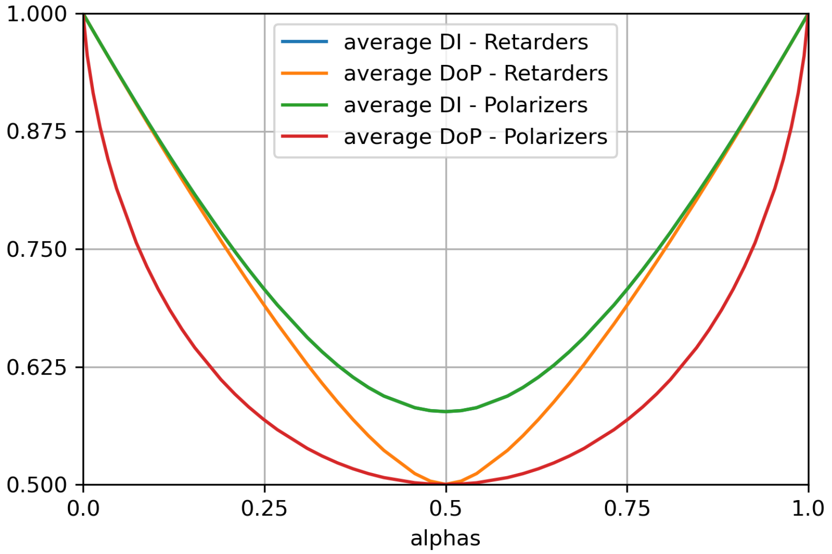

Figure 3.4: Overplotting the depolarization curves of Polarizers from the left side of Figure 3.1 with the curves of Retarders from the left side of Figure 3.3, it is easy to visualize the differences in behavior. The Depolarization Index (DI) is identical for two oppositely oriented linear polarizers and two opposite QWLR retarders. A change in behavior is seen in the Degree of Polarization. The retarders saw a much more linear decrease in average DoP compared to the parabolic nature of the polarizers.

Q is preserved in this frame as expected, and at no point is the exiting light fully transferred into Stokes U. The orthogonal polarization state is blocked.

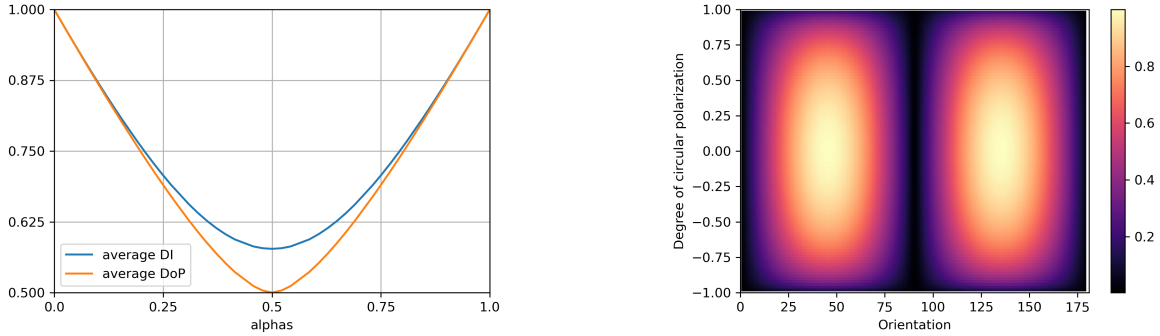

Figure 3.5: Shown here is a near identical scenario to the aperture in Figure 3.3. The only difference being that the QWLRs have both been rotated by 45°. The left plot remains unchanged from the HQWLR and VQWLR as the relative phase between the two retarders has not changed. However, in the plot of surface DoP on the right, a phase shift has occurred. The average DoP across the surface is completely polarized at 45° and 135° where Stokes U is preserved. And the surface is completely unpolarized at 0° and 90°, indicating Stokes Q is completely blocked.

We repeated this experiment after rotating both of the ideal QWLRs by 45°. This changes the orientation of the retarder's fast axis, changing the preserved quantity in this frame to be Stokes U. This should not effect the average DI or average DoP over the aperture, however, it should cause a phase shift in the DoP surface map. This is exactly what we see on the right side of Figure 3.5. In the DoP surface map for the rotated QWLR, the highest DoP occurs at 45° and 135° while there is no polarization at 0° and 90°.

3.2 Incorporating Mirror Coatings

Using the code described in Section 3.1, we added the calculation of a Mueller matrix using our Berreman code from Section 1.5. This allows the code to account for a potentially changing mirror coating at each point rather than using a fixed, known Mueller matrix, as with the polarizer and retarder tests.

In the first test configuration, a simulated mirror was split into two sections that covered a sliding fraction of the aperture with one section defined as α and the second as $1 - \alpha$. Each section was given a protected silver coating with varying layer thickness. Coating 1 covered a fraction α and was selected to be 5 nm of zinc sulfide (ZnS) over 115 nm of aluminum oxide (Al_2O_3). Coating 2 covered the remaining aperture, $(1-\alpha)$, and was selected to be 12 nm of ZnS over 100 nm of Al_2O_3. These coating thicknesses were chosen to be consistent with the thickest and thinnest lab metrology measurements of DKIST mirror witness samples. Bench-top spectropolarimetry measurements fit using a Berreman model (see Harrington et. al 2019, Fig. 29b)[13] and ellipsometry measurements taken over a range of angles both indicate this range of coating thicknesses and materials provide a representative coating model for DKIST mirrors.

Fifty-one model measurements were simulated with the top portion of the mirror "sliding down" between each step, decreasing the fraction covered by coating 1 and increasing the fraction of the aperture coated with coating 2. The aperture was uniformly illuminated with monochromatic light at a wavelength of 656.28 nm. In Figure 3.6, calculating the DI and average DoP for each sliding step, we see similar behavior as produced by a pair of linear polarizers or a pair of quarter wave linear retarders in Figures 3.1, 3.3, and 3.4. A mirror with an entirely uniform coating is non-depolarizing and the more non-uniform the coating the lower the DI and average DoP, with both DI and average DoP being minimized at $\alpha = 0.5$. However, for these coatings with ~ 5 nm differences in individual layer thickness, the depolarization effect is six orders of magnitude smaller than that of a pair of linear polarizers. From this, we can expect depolarization to be on the order of 10^{-6} for mirrors coated with the "DKIST protective silver."

The right side of Figure 3.6 shows the degree of polarization of light exiting the Mueller matrix of a simulated mirror where $\alpha = 0.5$. Orientation on the x-axis represents the direction of propagation of linear polarization as a function of angle where 0° is purely Stokes +Q and 45° is purely Stokes +U. On the y-axis the degree of circular polarization, or Stokes V, is shown. The surface contours of the plot represent how the exiting DoP is changing across the surface. When incoming linear polarization is purely Stokes Q (0° and 90°) and the circular component has low magnitude, no depolarization occurs (DoP = 1). The most depolarization occurs where linear polarization is fully in Stokes U (45°and 135°) though barely. The black regions indicate a DoP of 0.9995 or very slight depolarization.

The results of Figure 3.6 imply that depolarization is not a concern when the aperture is

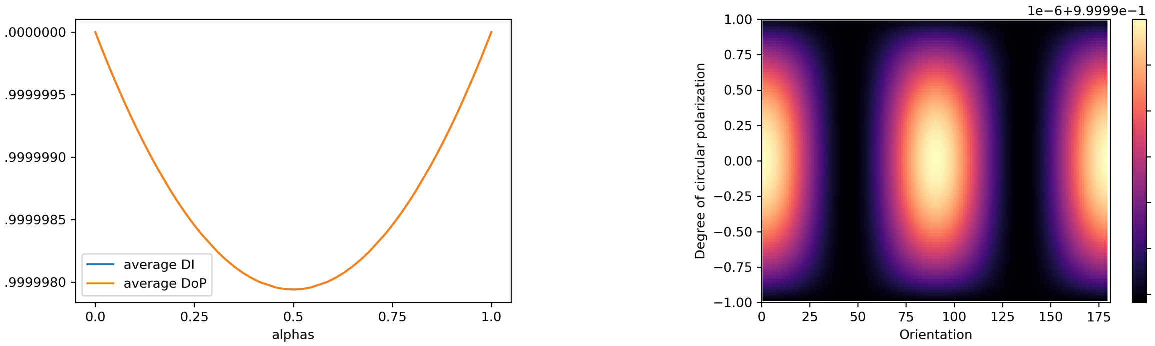

Figure 3.6: **Left:** A mirror where one fraction (α) of the aperture is coated with 5 nm ZnS over 115 nm Al_2O_3 and the rest of the aperture $(1 - \alpha)$ is coated with 12 nm ZnS over 100 nm of Al_2O_3 shows little depolarization (2×10^{-6}) across the average aperture at it's most non-uniform point $(\alpha = 0.5)$ An average DoP and DI near 1.0 both indicates the exiting beam is close to fully polarized. **Right:** A Degree of Polarization surface plot for $\alpha = 0.5$. The surface indicates how the exiting DoP is changing for different incoming polarization states. The most depolarization occurs when Stokes U $= \pm 1$ or Stokes V$= \pm 1$. At these points the exiting DoP $=\sim 0.9995$ or a very slight depolarization.

uniformly non-uniform, at least at a wavelength of 656.28 nm.

3.2.1 Expected Non-Uniformites in Coatings

In order to test the effects of coating non-uniformity on the magnitude of depolarization across an aperture, a zinc sulfide (ZnS) over aluminum oxide (Al_2O_3), protected silver mirror was modeled using Berreman calculus and varying layer thicknesses. The ZnS layer was defined as a defocused Zernike with thicknesses of 6 nm – 12 nm over the aperture and the Al_2O_3 layer was defined as a coating which mimics a vertical astigmatism Zernike with layer thickness of 100 nm – 115 nm as shown in Figure 3.7. Zernike polynomials were chosen for ease of use on a circular aperture and the Z_2^0 defocus and Z_2^2 astigmatism were chosen for their low order and resemblance to typical thin-film coating non-uniformites. The ZnS layer is approximating a coating that has been deposited such that it is thicker in the center than on the edges. The Al_2O_3 layer has been chosen to simulate a coating that is fairly uniform in the center with thicker and thinner non-uniformites on the edges. We have previously described spatial variations of substrate properties on DKIST and other telescope optics and refer the reader to Appendix B of Harrington et al. (2021)[28] for examples

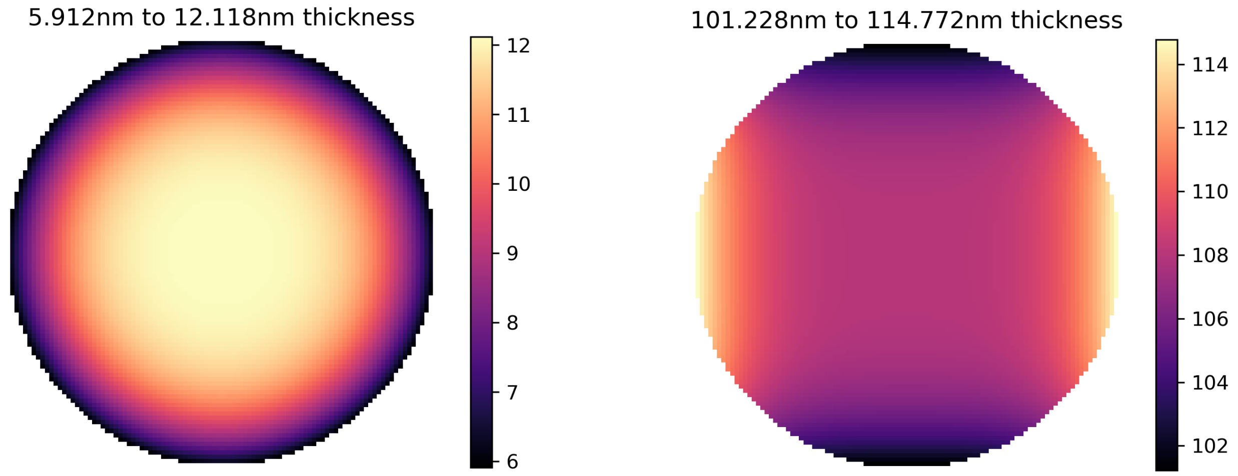
5.912nm to 12.118nm thickness

101.228nm to 114.772nm thickness

Figure 3.7: Model of a ZnS/Al_2O_3 mirror with non-uniform coating layers. Using DKIST mirror thickness ranges as a guide, Zernike polynomials were used to form gradients in the layer thicknesses. The left image shows the ZnS layer modeled as a Z_2^0 defocus Zernike with thicknesses ranging from 6 nm – 12 nm. The right image shows the Al_2O_3 layer modeled as a Z_2^2 vertical astigmatism Zernike with thicknesses ranging from 100 nm – 115 nm.

of spatial variation on real coatings. Thickness values were chosen to be consistent with our past findings for these mirror types which can be found in Figure 29 of Harrington et al. (2019).[13]

To predict the polarization properties of such a ZnS/Al_2O_3/Ag mirror, Berreman models were run at multiple angles of incidence (AOI) from 15° to 70° at every point on the aperture, which was illuminated with monochromatic light at a wavelength of 656.28 nm. The refractive index data used can be found in Boidin et al. (2016)[43] for Al_2O_3 and the TFCalc Software[47] for both ZnS and Ag. The polarization properties of reflectivity, retardance, and diattenuation are shown here in Figure 3.8 for the two extremes of the chosen incidence angle range. The top row shows small peak-to-valley variations across the aperture in both intensity and diattenuation (0.006, RMS = 0.001 and 0.012%, RMS = 0.002, respectively) at a shallow AOI of 15° with some non-uniformity in both properties occurring around the aperture edges. At the shown color scale, the retardance at 15° takes on a lobe like structure, however it is still fairly uniform with a small peak-to-valley variation of 0.2°(RMS = 0.043°) over the aperture. Average depolarization over the aperture is also very small (2.25×10^{-7}) as listed in Table 3.1.

AOI	**Avg DI**	**Avg DoP**	**1 − Avg DoP**
15°	0.9999998	0.9999997	2.3×10^{-7}
45°	0.99998	0.99998	2.4×10^{-5}
70°	0.99891	0.99905	9.5×10^{-4}

Table 3.1: Average DI, average DoP and aperture average depolarization over the aperture of the mirror modeled in Figures 3.7 and 3.8 at multiple AOIs. There is little polarization loss over the aperture from this particular non-uniformity.

From this, we again conclude that at small AOI, depolarization is not a concern for a single, flat, ZnS/Al_2O_3 protected silver mirrors with expected amounts of spatial variation across the aperture. Additionally, for the DKIST system, this estimate is well within the error budget described in Section 1.6.1.

In the bottom row of Figure 3.8, polarization properties are shown for a higher AOI at 70° incidence. While such a large angle is not present on DKIST, large angles are not uncommon on other astronomical telescopes. If we again look at reflectivity, retardance, and diattenuation over the aperture, the largest changes occur at the aperture edges in each with fairly uniform centers. The center retardance plot shows the largest change at a large angle with a peak-to-valley variation of 18.55° retardance which is twenty times larger than the 15° AOI variation. Some of this spread in retardance is expected due to the high AOI however it highlights how a large change in phase on the edges of the aperture can significantly increase the effects of depolarization which has increased by 3 magnitudes to 9.5×10^{-4} at 70° AOI.

3.2.2 A "Uniform" Mirror

To further test this result, another Zernike test was run where the range in layer thickness was constrained to be varying on the order of 10^{-6} nm to simulate a uniform mirror measured with noise perturbations. In this case, the ZnS layer was again represented by a defocus Zernike but had a layer thickness range of 5.9999983 nm − 6.00000173 nm and the Al_2O_3 was an astigmatism

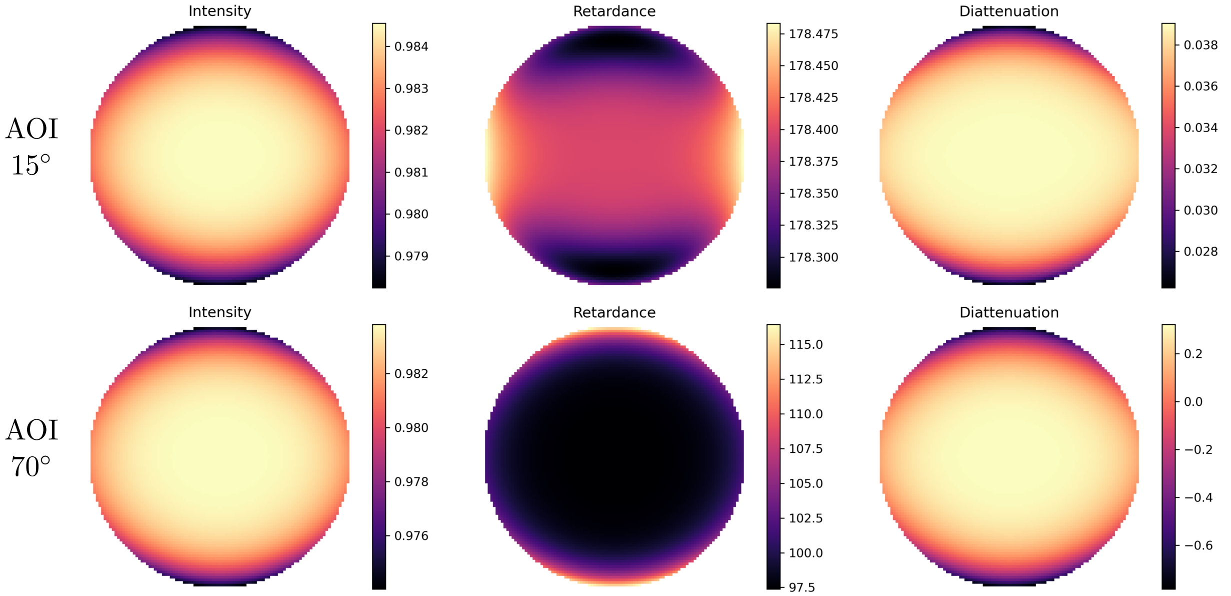

Figure 3.8: Intensity, retardance, and diattenuation across the aperture of the mirror model shown above at two different angle of incidences (AOI). At low AOI (top row, 15°), small peak-to-valley variations are seen across the aperture in intensity (0.006, RMS 0.001) and diattenuation (0.012%, RMS 0.002) with much of the non-uniformity around the aperture edges. Retardance across the aperture took on a lobe like appearance but still showed low variation with a peak-to-valley variation of 0.2°(RMS 0.043°). At high AOI (bottom row, 70°), a larger change in retardance over the aperture (18.55°peak-to-valley, RMS 3.34°) is seen however much of the variation is again at the edges of the aperture.

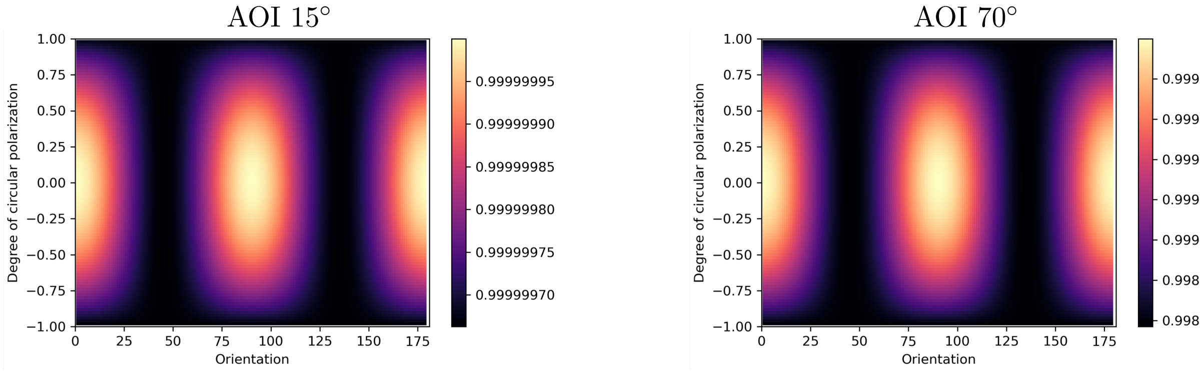

Figure 3.9: Over the DoP surface there is very little change in polarization. At 15° AOI (left), DoP varies in parts per million. At 70° AOI (right), DoP varies at the parts per 10,000 level for the same simulated mirror.

Zernike of thickness 107.99999378 − 108.00000622 nm. The resulting aperture average Mueller matrix for this surface was given by:

$$MM_{avg\ noise} = \begin{bmatrix} 0.9786 & 0.00250 & 0. & 0. \\ 0.00252 & 0.9786 & 0. & 0. \\ 0. & 0. & -0.27662 & -0.93869 \\ 0. & 0. & 0.93869 & -0.27662 \end{bmatrix}. \tag{3.4}$$

Compared to a completely uniform aperture, this noisy aperture presents excess retardance in the UV terms as can be seen by differencing the two Mueller matrices as follows:

$$MM_{avg\ noise} - MM_{uniform} = \begin{bmatrix} 0. & 0. & 0. & 0. \\ 0. & 0. & 0. & 0. \\ 0. & 0. & 3\times10^{-8} & -1\times10^{-8} \\ 0. & 0. & 1\times10^{-8} & 3\times10^{-8} \end{bmatrix}. \tag{3.5}$$

Given the polarimetric error budget in Equation 1.29, the excess retardance from such a mirror is well below the maximum uncertainty for each element of the system Mueller matrix.

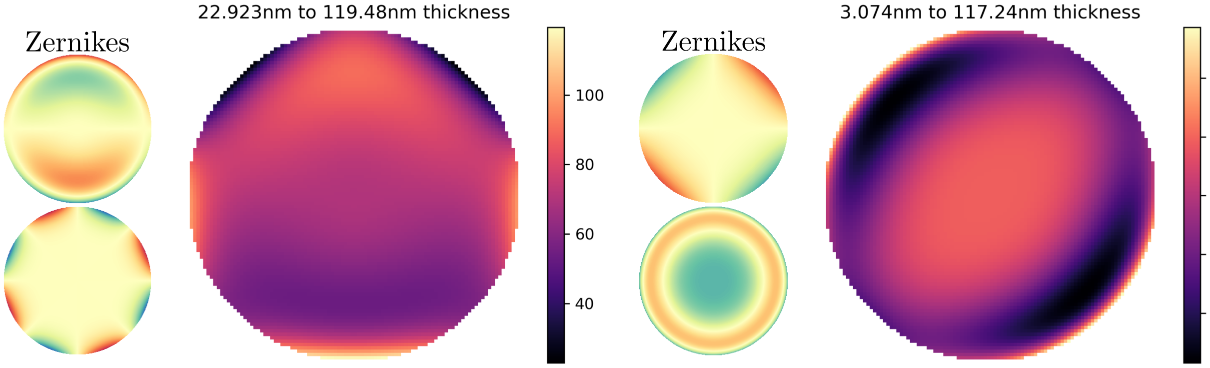

Figure 3.10: Model of a ZnS/Al_2O_3 mirror with very non-uniform coating layers. Zernike polynomials were again used to form a gradient of layer thicknesses with the intent to create an extreme range with structure on the aperture edges. The left image shows a new ZnS layer modeled as a higher order polynomial sum of Z^3_{-1} + Z^4_{-4} (coma + quadrafoil) with thicknesses ranging from 25 nm – 109 nm. The image on the right shows the Al_2O_3 layer modeled by the polynomial sum Z^4_{-2} + Z^4_0 (secondary astigmatism and spherical aberrations) with thicknesses ranging from 3 nm – to 110 nm. The individual Zernike functions used are shown besides each aperture.

3.2.3 Let's get Crazy! - Unrealistic coating non-uniformities

Section 3.2.1 modeled what a realistic non-uniform coating might look like. Here we simulate an exaggerated coating non-uniformity to explore how depolarization behavior might change given a large range of thickness variation and structure to the non-uniformity. For this experiment, we chose to use combinations of higher-order Zernikes to simulate variation across an aperture of arbitratry size as in Figure 3.10. The ZnS layer was modeled as a combination of the third-order vertical coma Zernike and fourth-order oblique quadrafoil Zernike polynomials with thickness ranging from 25 nm to 109 nm. This combination was chosen with the intent of simulating structure on the edges of the aperture as if the coating process had failed in some way. The Al_2O_3 layer was modeled as a combination of two fourth-order polynomials – secondary astigmatism and spherical aberrations. This layer has a thickness ranging from 3 nm to 110 nm with a thick central peak and two thinner lobes on the edges, as if the majority of material deposited contracted into the center of the optic.

This mirror configuration was run through the same Berreman simulation as the mirror described in Section 3.2.1 at AOIs of 15°, 30°, 45°, and 70°. Even with a non-uniform start, the

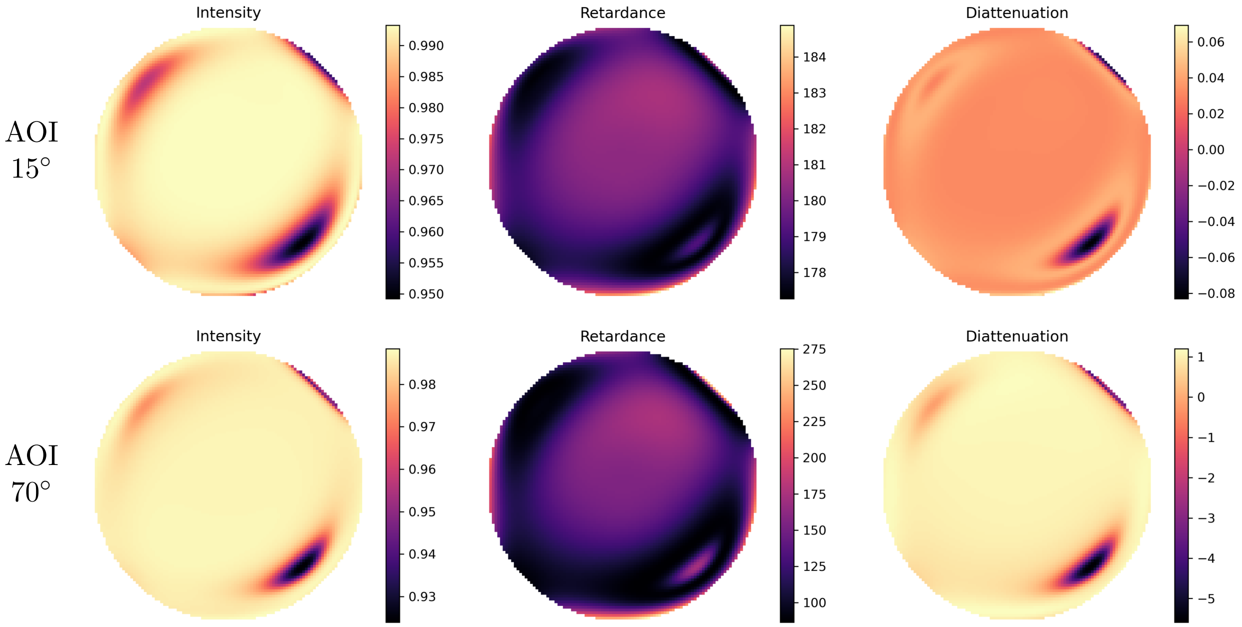

Figure 3.11: Intensity, retardance, and diattenuation across the aperture of the exaggeratedly non-uniform mirror model shown in Figure 3.10 at two different AOIs.

intensity and diattenuation over the aperture was fairly uniform for all AOIs as shown in Figure 3.11. At 15° AOI, intensity showed a peak-to-valley range of 0.05 and diattenuation a peak-to-valley range of 0.14%. At the largest AOI tested of 70°, differences in intensity were 0.06 peak-to-valley while diattenuation changed by 6% over the aperture. The biggest changes at all AOIs is again seen in the retardance term. There is similar structure to that is seen in the intensity and diattenuation, however the range of retardance values is 8° peak-to-valley at 15° AOI and 160° peak-to-valley at 70° AOI. Depolarization of the exiting beam increases by three orders of magnitude at each AOI as listed in Table 3.2. While designed to be a terrible representation of a mirror coating that might be used in an astronomical setting, this unrealistically non-uniform coating simulation demonstrates the magnitude of errors depolarization could cause if coating uniformity is left unchecked.

3.3 Summary

We showed here an example calculation of depolarization caused by non-uniform mirror coatings. We used a refractive index model based on our prior assessments of real mirror coatings.[12, 13, 28]

AOI	**Avg DI**	**Avg DoP**	**Min DoP**	**1 − Avg DoP**
15°	0.99989	0.99988	0.99983	1.2×10^{-4}
45°	0.98976	0.98916	0.985	1.08×10^{-2}
70°	0.92375	0.91701	0.882	8.3×10^{-2}

Table 3.2: Average DI and DoP over the aperture of the mirror modeled in Figures 3.10 and 3.11 at multiple AOIs. There is still small changes in the DoP over the surface for this very non-uniform mirror simulation. Compared to the mirror that was modeled to be of similar layer thickness as the DKIST mirrors in 3.1, this mirror is, on average, ~ 3 orders of magnitude more depolarizing.

Using the coating layer thickness variation estimates from our prior works, we showed examples of the non-uniform polarization response caused by variable coating-layer thickness. These simulations were done with a few common low-order Zernike modes at a few incidence angles to give a sense of the range of possible outcomes. DKIST telescope mirrors have incidence angles ranging from near zero to 45 degrees. At other astronomical telescope, in particular those with image de-rotators, can have much higher incidence angles. We showed calculations of the scalar Depolarization Index as well as examples of the depolarization over the full Poincaré sphere, covering all incident Stokes vectors. Depending on the incidence angle, coating uniformity, etc, the depolarization level expected for DKIST mirrors is at or below a few parts in ten thousand. These models add to the depolarization estimated in Harrington & Sueoka (2017)[12] for DKIST as the average over the aperture for a uniformly coated but curved optical surface. We contrast this level with the depolarization caused in the average over a converging beam footprint propagating through a retarder as simulated in Sueoka (2016).[57] With depolarization at these magnitudes, we can comfortably ignore depolarization as lower order of magnitude than other sources assuming the coating has be deposited reasonably uniformly and designed to be low retardance. It should also be noted that the results shown here are all for single, unpowered mirrors. The effects of depolarization will compound for a stack of mirrors in an optical path or for curved optics. Future work will pursue how the effects of depolarization changes as a many optic system, such as a telescope, changes pointings throughout observations. We will also be pursuing including this mirror coating depolarization behavior in future calibration techniques.

Chapter 4

Effects of mirror stacking and rotations: Application to DKIST

Using the simulations of mirrors with expected nonuniformities described in Section 3.2.1, we now explore what these mirrors look like stacked in a many-optic optical assembly with increasing complexity, gradually building to a DKIST-like system. All mirrors are still assumed to be flats with no curvature, and the full aperture is illuminated at a wavelength of 656.28 nm.

4.1 Simple stacks of mirrors within a system

We first started with a stack of ten mirrors with DKIST-like coatings and expected nonuniformities as described in Figure 3.7. All ten mirrors were positioned at 15° AOI in the optical train. This angle was chosen as the shallowest AOI in our simulations, and used here as it is representative of angles on the majority of optics found in the DKIST light distribution system (the Facility Instrument-Distribution Optics; FIDO[28]), and is at or within 5° of the incidence angles of five of the ten mirrors on DKIST. Table 4.1 lists the angles of incidence for mirrors on DKIST

Optic	M1	M2	M3	M4	M5	M6	M7	M8	M9	M10
AOI	14.04°	11.84°	45.0°	1.76°	15.0°	30.0°	45.0°	5.33°	10.0°	15.0°

Table 4.1: Angle of incidence for each of the 10 mirrors on DKIST.[12,24] With the exception of M1, all of these mirrors are coated with "DKIST Silver." The primary mirror of DKIST, M1, is coated with bare Al, however all mirrors in the models presented here are assumed to be coated with a protective silver.

as traced through the system by the chief ray.

The normalized Mueller matrix for one such a mirror is given by:

$$\mathbf{M}_{\text{AOI }15^\circ} = 0.98329 \times \begin{bmatrix} 1.0 & -3.7\times10^{-4} & 0. & 0. \\ -3.7\times10^{-4} & 1.0 & 0. & 0. \\ 0. & 0. & -0.9996 & -0.02836 \\ 0. & 0. & 0.02836 & -0.9996 \end{bmatrix}. \tag{4.1}$$

Reading this matrix as described in Equation 1.11, the average reflectivity of the aperture was above 98%, as expected for a protected silver coating. From the QI term, diattenuation loss was at -0.037%. Computing retardance using Equation 1.13, we find that the retardance of the single mirror to be minimal at 178.38° ($\sim 2^\circ$ from ideal).

Stacking ten of these mirrors in an optical train all set to 15° incidence and assuming no rotations or changes in the nonuniformities across the apertures resulted in the following normalized Mueller matrix to describe the system:

$$\mathbf{M}_{\text{AOI }15^\circ,\ 10} = 0.84494 \times \begin{bmatrix} 1.0 & -0.00374 & 0. & 0. \\ -0.00374 & 1.0 & 0. & 0. \\ 0. & 0. & 0.96005 & 0.27981 \\ 0. & 0. & -0.27981 & 0.96005 \end{bmatrix}. \tag{4.2}$$

We see an expected loss of reflectivity (84.5% compared to the previous 98.3%) and a 10% increase in diattenuation at -0.37% for stacked mirrors. The largest change in polarization properties occurred in the retardance which was 163.75° (a decrease of $\sim 14.6^\circ$) for the ten mirrors in succession. One caveat to these results is that the primary mirror, M1, on DKIST is coated with bare Al, which has a lower reflectivity than protected silver. The average reflectivity of an Al mirror followed by nine Ag mirrors will be slightly lower than the estimates given here for a stack of ten Ag mirrors. In terms of depolarization, the average DI and average DoP differ by an order of magnitude between the single-mirror and stacked-mirror cases. These values are summarized in Table 4.2.

AOI		**Reflectance**	**D**	δ	**Avg DI**	**Avg DoP**	**1 − Avg DoP**
15°	1 mirror	98.3%	-0.037%	178.38°	0.9999998	0.9999998	1.93×10^{-7}
	10 mirrors	84.5%	-0.37%	163.75°	0.9999981	0.999998	1.93×10^{-6}
45°	1 mirror	98.07%	-0.269%	158.31°	0.99997	0.99997	2.38×10^{-5}
	10 mirrors	82.3%	-2.69%	143.09°	0.9997	0.9997	2.38×10^{-4}
70°	1 mirror	98.23%	-0.15%	99.76°	0.9989	0.9989	1.09×10^{-3}
	10 mirrors	83.66%	-1.50%	97.61°	0.9892	0.9892	1.08×10^{-2}

Table 4.2: A comparison of reflectance and polarization properties for a single mirror at different AOIs and a series of ten mirrors, all at the same AOI, stacked together. At all angles, the reflectance decreased as expected for a series of Ag mirrors. Diattenuation (**D**), average depolarization index (DI), and the average degree of polarization (DoP) increased by an order of magnitude. This was expected as each mirror is identical and contributing the same amount of depolarization to the final image.

Repeating the above exercise of stacking mirrors but with AOIs of 45° and 70°, we find a similar behavior to an AOI of 15°. As with the mirrors at 15°, retardance dropped by $\sim 15°$ when ten mirrors were stacked at both AOIs. Diattenuation and average DoP increased by an order of magnitude, as expected. As identical mirrors are being stacked, each mirror contributes the same amount of depolarization to the end result. The Muller matrices for these mirrors are detailed in Equations 4.3−4.6 at the end of this chapter.

Differences in depolarization results from Chapter 3

The values listed in Tables 3.1 and 4.2 are slightly different between the two simulations. While small (See Table 4.3), these discrepancies bring forward an interesting discussion on when in the process an average over the aperture should be taken. The expected non-uniformity tests described in Section 3.2.1 were concerned with changes across the aperture of the entire mirror. To evaluate those changes, a Mueller matrix was calculated at each point and then used as a transfer matrix for all possible incoming Stokes vectors. The resulting outgoing Stokes vectors were then averaged over the aperture and used to compute a surface DoP. On the other hand, when simulating stacking mirrors, a single Mueller matrix representing the aperture average was used. This was done to limit computation time, however, means smaller non-uniformities may not be wholly accounted for. Depending on the level of precision required for a polarimetry result, it may be more accurate to track every individual point across all apertures before computing the depolarization, though this is likely only an issue for many-optic systems and large AOIs.

4.2 Mirror stacks at DKIST angles

Continuing to add complexity to this model, the next step we took was to implement the DKIST incidence angles listed in Table 4.1. The same 2-layer simulated mirror described in Figure 3.7 was used again to represent each of the ten facility mirrors on DKIST. A Berreman model was made for the mirror at each point on the aperture and at each angle. All of the mirrors were then stacked by matrix-multiplying each to obtain the total aperture of the system. All possible Stokes

$1 -$ Avg DoP Results			
AOI	**Non-uniformity tests**	**Stacking tests**	**|Difference|**
15°	2.3×10^{-7}	1.93×10^{-7}	3.7×10^{-8}
45°	2.4×10^{-5}	2.38×10^{-5}	2×10^{-7}
70°	9.5×10^{-4}	1.09×10^{-3}	1.40×10^{-4}

Table 4.3: The different models presented in Sections 3.2.1 and 4.1 for a single mirror at different AOIs yield slightly different results due to differences in how they were calculated. While small in magnitude, depending on the level of precision necessary for a polarimetry result, averaging over the aperture later in the calculation and increased computation time may be necessary.

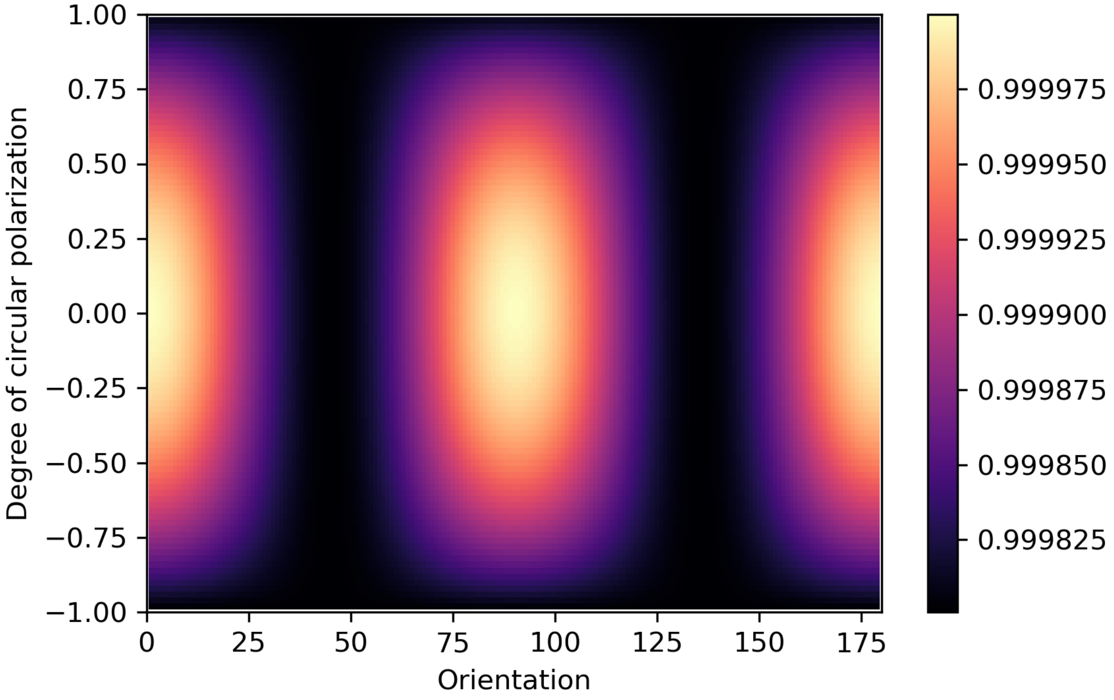

Figure 4.1: Here we show the surface Degree of Polarization for all possible incident Stokes vectors for the stack of mirrors positioned at DKIST AOIs. The minimum DoP over the surface is 0.9998. The average DoP over the surface is marginally higher at 0.999867, yielding an average depolarization of 1.33×10^{-4}.

vectors were then applied to the resulting aperture, and the outgoing Stokes vector was used to compute the final DoP and DI.

We found minimal depolarization for the DKIST-angle stack of mirrors at a wavelength of $\lambda = 656.28$ nm. The minimum value of surface DoP over the Poincaré sphere is .9998 in the ±U directions, as shown in Figure 4.1, which is a maximum depolarization of 1.999×10^{-4} depending on the incident polarization state. The average depolarization over the aperture is 1.33×10^{-4}, which is the same order of magnitude of the depolarization seen in the stack of mirrors with all AOIs set to 45°.

Stacked AOIs	**Avg DI**	**Avg DoP**	**1 − Avg DoP**
15°	0.9999981	0.999998	1.93×10^{-6}
45°	0.9997	0.9997	2.38×10^{-4}
DKIST AOIs	0.999	0.999867	1.33×10^{-4}

Table 4.4: A summary of depolarization metrics for 10 stacked mirrors at different AOIs at a wavelength of $\lambda = 656.28$ nm. The average depolarization values listed in the last column are the same order of magnitude or smaller than the tolerances set by the DKIST error matrix (Equation 1.29).

4.3 Summary and Next Steps

The preliminary results here show that any system-induced polarization originating from mirrors is small for this particular wavelength. We found the average depolarization across the final aperture of a stack of ten mirrors to be of order 10^{-4} at DKIST AOIs and when all ten mirrors are positioned at 45° incidence, well within the tolerances of the error matrix outlined in Equation 1.29. Next steps in building up this model include adding rotations to mimic the elevation and azimuth axes of the telescope. Other wavelengths at which DKIST observes will also need to be checked for consistency. We will also be changing the simulated mirror coating to utilize NLSP data derived Mueller matrices from measurements of witness samples rather than theoretical coatings. Powered optics will be the last puzzle piece to be implemented as the model will need to be transferred into a ray tracing program.

Muller Matrices referenced in Section 4.1

The following Mueller matrices are all normalized to the II intensity term. They have been computed and interpreted identically to the 15° detailed above. These matrices are presented here for posterity.

Single Ag mirror at 45°

$$\mathbf{M}_{\text{AOI }45^\circ} = 0.9807 \times \begin{bmatrix} 1.0 & -0.00269 & 0. & 0. \\ -0.00269 & 1.0 & 0. & 0. \\ 0. & 0. & -0.9292 & -0.3696 \\ 0. & 0. & 0.3696 & -0.9292 \end{bmatrix}. \tag{4.3}$$

10 Ag mirrors naïvely stacked, all at 45°

$$\mathbf{M}_{\text{AOI }45^\circ,\ 10} = 0.8230 \times \begin{bmatrix} 1.0 & -0.02688. & 0. & 0. \\ -0.02688. & 1.0. & 0. & 0. \\ 0. & 0. & -0.79905 & -0.60007 \\ 0. & 0. & 0.60007 & -0.79905 \end{bmatrix}. \tag{4.4}$$

Single Ag mirror at AOI 70°

$$\mathbf{M}_{\text{AOI }70^\circ} = 0.9823 \times \begin{bmatrix} 1.0 & -0.0015 & 0. & 0. \\ -0.0015 & 1.0 & 0. & 0. \\ 0. & 0. & -0.1693 & -0.9839 \\ 0. & 0. & 0.9839 & -0.1693 \end{bmatrix}. \tag{4.5}$$

10 Ag mirrors naïvely stacked, all at 70°

$$\mathbf{M}_{\text{AOI }70^\circ,\ 10} = 0.8366 \times \begin{bmatrix} 1.0 & -0.015. & 0. & 0. \\ -0.015. & 1.0. & 0. & 0. \\ 0. & 0. & 0.1303 & 0.9750 \\ 0. & 0. & -0.9750 & 0.1303 \end{bmatrix}. \tag{4.6}$$

Chapter 5

Conclusions and next steps

As science goals drive cutting-edge instrumentation, calibration methods on those instruments must also evolve to meet performance requirements. We have shown how current polarization calibration methods can be improved by providing more realistic inputs to the system models that are used in the calibrations. Through careful metrology work and a reassessment of what can or cannot be ignored in polarization calibrations, new levels of precision and accuracy can be achieved.

In Chapter 2, we expanded on the work of Harrington et al. (2019)[13] by using the Berreman calculus described in Section 1.5 to fit NLSP data of various mirror witness samples from DKIST and other solar telescopes. These new fits utilized both retardance and diattenutation data instead of just retardance. The optimizer `scipy.optimize.differential_evolution()` was also implemented to easily allow for the new fit parameters. We also removed any dependence on proprietary coating formulas or on reliable refractive-index dispersion curves by adding a new module that fits for the refractive index of a dielectric coating using a Cauchy equation. Future work should focus on fitting the metal layer of a mirror coating. The fitting code is now capable of deriving a model for any individual optic without knowing anything a priori about the coating.

Chapter 3 explored the loss of polarization by an optic due to non-uniformly applied coatings. Most system models, including DKIST's, assume depolarization is small compared to other instrument errors and systematics and ignore it. We simulated a DKIST-like mirror with data from the fits in Chapter 2 and predict the magnitude of depolarization caused by a non-uniformly coated mirror. We found that the depolarization of a single flat mirror, with DKIST-like coating thicknesses ranges from $\sim 10^{-5}$ to $\sim 10^{-7}$ depending on the angle of incidence of the incoming light. These values are well below the tolerance levels that DKIST requires in the calibration error matrix (Equation 1.29). Even for very poorly coated optics where coating thickness changes non-uniformity by 100 nm over the aperture, we find the induced depolarization to be close but still below tolerance limits; a range of $\sim 10^{-2}$ to $\sim 10^{-4}$ depending on the angle of incidence. We concluded that, for a single mirror, depolarization from non-uniform coatings is negligible. Chapter 4 expanded on this by 'stacking' a series of ten mirrors to predict the compounded depolarization that maybe induced by a many optic system, like a 4m telescope. We predict that for a stack of flat mirrors set at the same angles of incidence used by DKIST the mirror-induced depolarization will still be below DKIST's required tolerance by two orders of magnitude that we estimate to be $\sim 10^{-4}$. Future work should include powered optics, which will further increase the depolarization. Previous work by Harrington and Sueoka (2017)[12] estimated the depolarization at DKIST's Gregorian focus to originate from averaging over the aperture and be at a level of $\sim 0.1\%$ for the on-axis, zero field beam and 10^{-5} for a 5-arc minute field of view. Given these estimates, further work has not yet been done.

5.1 Future Work

This thesis presents an advancement of our understanding of the polarization systematics introduced by individual optics. Still, this work will benefit from further exploration of three different areas: the impact of diattenuation in determining refractive index; the effect of curved optics; and polarization wavelength dependence.

5.1.1 Modeling of coatings

The model fits described in Chapter 2 still have several limitations that can be expanded upon. Currently, only the dielectric layers that enhance a mirror coating are fit for. The metal layer is given a set thickness and uses a lookup table to determine the refractive index for given wavelength. As plotted in Figure 2.15, we have attempted to model the real component of the refractive index as a parabola to minimize the number of parameters we fit. However, this does not replicate the correct form of refractive indices found in the literature. A more suitable polynomial has not yet been determined. We have inferred from Figure 2.7 that the metal layer drives the level of diattenuation. This is likely to vastly improve our models as, even with the addition of diattenuation to minimization of the error used to determine the fit, diattenuation data are poorly matched.

The weighting of diattenuation in the error metric should also improve the fit of the model to the data. Diattenuation has been added to Equation 2.1 however it is currently considered to be equal to the level of retardance. When minimizing a model fit, trial-and-error indicates that retardance should be more heavily weighted, however, by how much has not been determined. It may not be possible to confidently determine a weighting before fits to the metal layer adds additional degrees of freedom to the fit.

5.1.2 Mirror induced depolarization

Chapters 3 and 4 both added to the complexity of a simple optical system, but other factors must still be added to fully represent a realistic scenario. The models described assume that each mirror is a simple flat-fold and fully illuminated. Real optical systems use curved optics to manipulate a beam that propagates through the system. An articulated system will have optics rotating against each other. Both of these scenarios will require the inclusion of field angles and changes to where is illuminated on a given mirror, and any local non-uniformites in the coating.

Additionally, everything described in Chapters 3 and 4 was done at a single wavelength. Ideally, the full wavelength range of DKIST, from 380 nm to 5 μm, would be analyzed to determine if all observations will be below the allowed error tolerance. An initial look at the wavelength dependence is described in the next section.

5.2 Impact on DKIST

To get a sense of if there is a wavelength dependence to depolarization, we selected seven wavelengths of importance from cases in the DKIST Critical Science Plan[26] and reran the analysis carried out in Section 4.2 for stacks of ten mirrors in two scenarios: with all mirrors set to 45° AOI and with mirrors at DKIST angles (Table 4.1). A summary of the results is presented in Table 5.1.

Two of the studied wavelengths, both Ca II lines, stand out as potentially problematic and are highlighted in bold. The Ca II H, K and Ca II IR lines are used in chromospheric studies of magnetic fields and will be observed by three of the four first-light polarimeters on DKIST – ViSP, VTF and DL-NIRSP.[26,30–32] We estimate that the depolarization of a stack of ten mirrors at DKIST angles is of the order of magnitude 10^{-2}, which is the same order of magnitude as the error tolerances listed in the DKIST error matrix (Equation 1.29). We also expect there to be more depolarization once system articulation and mirror curvature are taken into account. Given that depolarization induced by mirror coatings is completely excluded from the current DKIST polarization system model[25] and estimates are at the allowed error tolerance without considering any other sources of systematics, we conclude that DKIST observations near 397 nm and 854 nm will need more study and special characterization. Given the importance of Ca II lines to constraining temperatures in the chromosphere, a study of the error matrix at these specific wavelengths is recommended. It is possible that this result highlights a need for a wavelength dependent error-matrix across the entire bandpass observed by DKIST. It is also worth noting that the models presented here include all 10 system mirrors in the depolarization error estimate. Currently, all optics located in the coudé laboratory, M7 through the instruments, are fit to the modulation matrix of the system which *does* account for the depolarization.[25,38] This means that the models here are most likely an overestimate of depolarization caused by system mirrors. As M7 is positioned at a fixed angle of 45°, it has a large impact on the estimates presented here; however, it is accounted for elsewhere in the system model. Repeating the analysis presented here with mirrors M1 through M6 is recommend before any further changes are made.

Line	AOI	Avg DoP	Depolarization
Ca II K	45°	0.8785	1.215×10^{-1}
396.85 nm	**DKIST**	**0.9856**	$\mathbf{1.44 \times 10^{-2}}$
Fe XIV	45°	0.9777	2.22×10^{-2}
530.3 nm	DKIST	0.998	1.87×10^{-3}
Ne laser	45°	0.9985	1.46×10^{-3}
633.443 nm	DKIST	0.9998	1.60×10^{-4}
Hα	45°	0.9978	2.20×10^{-3}
656.28 nm	DKIST	0.9999	1.29×10^{-4}
Ca II	45°	0.8259	1.74×10^{-1}
854.2 nm	**DKIST**	**0.9838**	$\mathbf{1.62 \times 10^{-2}}$
He I triplet	45°	0.9562	4.38×10^{-2}
1080 nm	DKIST	0.9956	4.38×10^{-3}
CO bands	45°	0.9996	4.37×10^{-4}
4666 nm	DKIST	0.99997	1.08×10^{-5}

Table 5.1: A summary of depolarization metrics for various wavelengths that are important to DKIST science objectives. Each row represents a 10-mirror stack where the AOI of all mirrors are set to 45° or the DKIST AOIs listed in Table 4.1 are used. The Ca II lines in both the UV and IR are highlighted as being of the same magnitude as the allowed error tolerances. This could be problematic if depolarization estimates increase as expected with the inclusion of telescope articulation and powered optics.

5.3 Summary

The fields of solar and astrophysics are constantly pushing the technological boundaries of optical systems to further tighten and constrain our understanding of physical phenomena. This requires careful and precise calibration of instrument hardware to ensure the accuracy of the resulting physical inferences. Although the work presented in this thesis was developed for DKIST and its optical train, it is important to reiterate that it can be extrapolated to any optical system requiring polarization calibration. For example, in Chapter 2 our analysis was conducted with optical coatings from the GREGOR telescope, and it can also be applied to and benefit other upcoming major observatories such as the Thirty Meter Telescope (TMT) and the European Solar Telescope (EST).

Bibliography

[1] Porter, R. W., [Amateur Telescope Making], Scientific American Publishing Company (1926).

[2] del Toro Iniesta, J. C. and Ruiz Cobo, B., "Inversion of the radiative transfer equation for polarized light," Living Reviews in Solar Physics **13**, 4 (Nov. 2016).

[3] Breckinridge, J. B., [Basic optics for the astronomical sciences], SPIE Press, Bellingham, Wash (2012).

[4] Chipman, R. A., Young, G., and Lam, W. S. T., [Polarized light and optical systems], Optical sciences and applications of light, Taylor & Francis, CRC Press, Boca Raton (2018).

[5] Goldstein, D. H., [Polarized Light], CRC Press (Dec. 2017).

[6] Azzam, R. M. A. and Bashara, N. M., [Ellipsometry and polarized ligth], North-Holland personal library, North-Holland, Amsterdam London New York [etc.] (1992).

[7] McCall, M. W., Hodgkinson, I. J., and Wu, Q., [Birefringent Thin Films and Polarizing Elements], Imperial College Press, London, 2nd edition ed. (2015).

[8] del Toro Iniesta, J. C., [Introduction to Spectropolarimetry], Cambridge University Press, Cambridge (2003).

[9] Clarke, D., [Stellar polarimetry], Wiley-VCH, Weinheim (2010). OCLC: ocn489628079.

[10] Degl'Innocenti, E. L. and Landolfi, M., [Polarization in spectral lines], no. v. 307 in Astrophysics and space science library, Kluwer Academic Publishers, Dordrecht ; Boston (2004). OCLC: ocm55633773.

[11] Trujillo Bueno, J., Moreno-Insertis, F., and Sánchez, F., eds., [Astrophysical spectropolarimetry: proceedings of the XII Canary Islands Winter School of Astrophysics, Puerto de la Cruz, Tenerife, Spain, November 13-24, 2000], Cambridge University Press, Cambridge ; New York (2002). Meeting Name: Canary Islands Winter School on Astrophysics.

[12] Harrington, D. M. and Sueoka, S. R., "Polarization modeling and predictions for Daniel K. Inouye Solar Telescope part 1: telescope and example instrument configurations," Journal of Astronomical Telescopes, Instruments, and Systems **3**, 018002 (Feb. 2017).

[13] Harrington, D. M., Sueoka, S. R., and White, A. J., "Polarization modeling and predictions for Daniel K. Inouye Solar Telescope part 5: impacts of enhanced mirror and dichroic coatings on system polarization calibration," Journal of Astronomical Telescopes, Instruments, and Systems **5**, 038001 (June 2019).

[14] Lu, S.-Y. and Chipman, R. A., "Interpretation of Mueller matrices based on polar decomposition," Journal of the Optical Society of America A **13**, 1106 (May 1996).

[15] Harrington, D. M., Kuhn, J. R., and Ariste, A. L., "Daytime sky polarization calibration limitations," Journal of Astronomical Telescopes, Instruments, and Systems **3**, 018001 (Jan. 2017).

[16] Landstreet, J. D., "Basics of spectropolarimetry," Proceedings of the International Astronomical Union **9**, 311–320 (June 2014).

[17] Macleod, H. A., [Thin-film optical filters], Series in optics and optoelectronics, CRC Press, Taylor & Francis Group, Boca Raton, fifth edition ed. (2018).

[18] Pelletier, E., "Methods for Determining Optical Parameters of Thin Films," in [Handbook of Optical Constants of Solids], 57–73, Elsevier (1998).

[19] Hecht, E., [Optics], Pearson Education, Inc, Boston, 5 ed ed. (2017).

[20] "Understanding Thin Film Process Technologies, REO Inc.." `https://www.reoinc.com/technical-resources/cat/78/technical-tutorials/article/Coating-Process-Tutorial`. Date accessed, 2018-09-09.

[21] Teitler, S. and Henvis, B. W., "Refraction in Stratified, Anisotropic Media*," Journal of the Optical Society of America **60**, 830 (June 1970).

[22] Berreman, D. W., "Optics in Stratified and Anisotropic Media: 4×4-Matrix Formulation," JOSA **62**, 502–510 (Apr. 1972).

[23] Jones, R. C., "A New Calculus for the Treatment of Optical SystemsI. Description and Discussion of the Calculus," JOSA **31**, 488–493 (July 1941).

[24] Rimmele, T. R., Warner, M., Keil, S. L., Goode, P. R., Knölker, M., Kuhn, J. R., Rosner, R. R., McMullin, J. P., Casini, R., Lin, H., Wöger, F., von der Lühe, O., Tritschler, A., Davey, A., de Wijn, A., Elmore, D. F., Fehlmann, A., Harrington, D. M., Jaeggli, S. A., Rast, M. P., Schad, T. A., Schmidt, W., Mathioudakis, M., Mickey, D. L., Anan, T., Beck, C., Marshall, H. K., Jeffers, P. F., Oschmann, J. M., Beard, A., Berst, D. C., Cowan, B. A., Craig, S. C., Cross, E., Cummings, B. K., Donnelly, C., de Vanssay, J.-B., Eigenbrot, A. D., Ferayorni, A., Foster, C., Galapon, C. A., Gedrites, C., Gonzales, K., Goodrich, B. D., Gregory, B. S., Guzman, S. S., Guzzo, S., Hegwer, S., Hubbard, R. P., Hubbard, J. R., Johansson, E. M., Johnson, L. C., Liang, C., Liang, M., McQuillen, I., Mayer, C., Newman, K., Onodera, B., Phelps, L., Puentes, M. M., Richards, C., Rimmele, L. M., Sekulic, P., Shimko, S. R., Simison, B. E., Smith, B., Starman, E., Sueoka, S. R., Summers, R. T., Szabo, A., Szabo, L., Wampler, S. B., Williams, T. R., and White, C., "The Daniel K. Inouye Solar Telescope - Observatory Overview," Solar Physics **295**, 172 (Dec. 2020).

[25] Harrington, D. M., Sueoka, S. R., Schad, T. A., Beck, C., Eigenbrot, A. D., De Wijn, A. G., Casini, R., White, A. J., and Jaeggli, S. A., "Systems Approach to Polarization Calibration for the Daniel K. Inouye Solar Telescope (DKIST)," Solar Physics **298**, 10 (Jan. 2023).

[26] Rast, M. P., Bello González, N., Bellot Rubio, L., Cao, W., Cauzzi, G., DeLuca, E., De Pontieu, B., Fletcher, L., Gibson, S. E., Judge, P. G., Katsukawa, Y., Kazachenko, M. D., Khomenko,

E., Landi, E., Martínez Pillet, V., Petrie, G. J. D., Qiu, J., Rachmeler, L. A., Rempel, M., Schmidt, W., Scullion, E., Sun, X., Welsch, B. T., Andretta, V., Antolin, P., Ayres, T. R., Balasubramaniam, K. S., Ballai, I., Berger, T. E., Bradshaw, S. J., Campbell, R. J., Carlsson, M., Casini, R., Centeno, R., Cranmer, S. R., Criscuoli, S., DeForest, C., Deng, Y., Erdélyi, R., Fedun, V., Fischer, C. E., González Manrique, S. J., Hahn, M., Harra, L., Henriques, V. M. J., Hurlburt, N. E., Jaeggli, S., Jafarzadeh, S., Jain, R., Jefferies, S. M., Keys, P. H., Kowalski, A. F., Kuckein, C., Kuhn, J. R., Kuridze, D., Liu, J., Liu, W., Longcope, D., Mathioudakis, M., McAteer, R. T. J., McIntosh, S. W., McKenzie, D. E., Miralles, M. P., Morton, R. J., Muglach, K., Nelson, C. J., Panesar, N. K., Parenti, S., Parnell, C. E., Poduval, B., Reardon, K. P., Reep, J. W., Schad, T. A., Schmit, D., Sharma, R., Socas-Navarro, H., Srivastava, A. K., Sterling, A. C., Suematsu, Y., Tarr, L. A., Tiwari, S., Tritschler, A., Verth, G., Vourlidas, A., Wang, H., Wang, Y.-M., NSO, and DKIST instrument scientists, D. p., the DKIST Science Working Group, and the DKIST Critical Science Plan Community, "Critical Science Plan for the Daniel K. Inouye Solar Telescope (DKIST)," Solar Physics **296**, 70 (Apr. 2021).

[27] Fehlmann, A., Kuhn, J. R., Schad, T. A., Scholl, I. F., Williams, R., Agdinaoay, R., Berst, D. C., Craig, S. C., Giebink, C., Goodrich, B., Hnat, K., James, D., Lockhart, C., Mickey, D. L., Oswald, D., Puentes, M. M., Schickling, R., De Vanssay, J.-B., and Warmbier, E. A., "The Daniel K. Inouye Solar Telescope (DKIST) Cryogenic Near-Infrared Spectro-Polarimeter," Solar Physics **298**, 5 (Jan. 2023).

[28] Harrington, D. M., Wöger, F., White, A. J., and Sueoka, S. R., "Polarization modeling and predictions for DKIST, part 9: flux distribution with FIDO," Journal of Astronomical Telescopes, Instruments, and Systems **7**, 048005 (Dec. 2021). Publisher: SPIE.

[29] Wöger, F., Rimmele, T., Ferayorni, A., Beard, A., Gregory, B. S., Sekulic, P., and Hegwer, S. L., "The Daniel K. Inouye Solar Telescope (DKIST)/Visible Broadband Imager (VBI)," Solar Physics **296**, 145 (Oct. 2021).

[30] de Wijn, A. G., Casini, R., Carlile, A., Lecinski, A. R., Sewell, S., Zmarzly, P., Eigenbrot, A. D., Beck, C., Wöger, F., and Knölker, M., "The Visible Spectro-Polarimeter of the Daniel K. Inouye Solar Telescope," Solar Physics **297**, 22 (Feb. 2022).

[31] Jaeggli, S. A., Lin, H., Onaka, P., Yamada, H., Anan, T., Bonnet, M., Ching, G., Huang, X.-P., Kramar, M., McGregor, H., Nitta, G., Rae, C., Robertson, L., Schad, T. A., Toyama, P., Young, J., Berst, C., Harrington, D. M., Liang, M., Puentes, M., Sekulic, P., Smith, B., and Sueoka, S. R., "The Diffraction-Limited Near-Infrared Spectropolarimeter (DL-NIRSP) of the Daniel K. Inouye Solar Telescope (DKIST)," Solar Physics **297**, 137 (Oct. 2022).

[32] von der Lühe, O. and et al., "The DKIST visible tunable filter," Solar Physics **296**, in preperation (2023).

[33] Rimmele, T. R. and The ATST Science Working Group, "Science Requirements Document," Tech. Rep. DKIST Project Documentation SPEC-0001. (2005). `https://nso.edu/wp-content/uploads/2020/10/SPEC-0001_SRD_RevB.pdf`.

[34] Harrington, D. M., Snik, F., Keller, C. U., Sueoka, S. R., and Harten, G. v., "Polarization modeling and predictions for DKIST part 2: application of the Berreman calculus to spectral polarization fringes of beamsplitters and crystal retarders," Journal of Astronomical Telescopes, Instruments, and Systems **3**, 048001 (Oct. 2017).

[35] Harrington, D. M. and Sueoka, S. R., “Polarization modeling and predictions for DKIST part 3: focal ratio and thermal dependencies of spectral polarization fringes and optic retardance,” Journal of Astronomical Telescopes, Instruments, and Systems **4**, 018006 (Mar. 2018).

[36] Harrington, D. M. and Sueoka, S. R., “Polarization modeling and predictions for Daniel K. Inouye Solar Telescope part 4: calibration accuracy over field of view, retardance spatial uniformity, and achromat design sensitivity,” Journal of Astronomical Telescopes, Instruments, and Systems **4**, 044006 (Dec. 2018).

[37] Harrington, D., Jaeggli, S. A., Schad, T. A., White, A. J., and Sueoka, S. R., “Polarization modeling and predictions for Daniel K. Inouye Solar Telescope, part 6: fringe mitigation with polycarbonate modulators and optical contact calibration retarders,” Journal of Astronomical Telescopes, Instruments, and Systems **6**, 038001 (July 2020). Publisher: International Society for Optics and Photonics.

[38] Harrington, D. M., Sueoka, S., White, A. J., Eigenbrot, A., and Schad, T., “Polarization modeling and predictions for Daniel K. Inouye Solar Telescope, part 7: preliminary NCSP system calibration and model fitting,” Journal of Astronomical Telescopes, Instruments, and Systems **7**, 018004 (Mar. 2021). Publisher: International Society for Optics and Photonics.

[39] Harrington, D. M., Schad, T., Sueoka, S., and White, A. J., “Polarization modeling and predictions for DKIST, part 8: calibration polarizer spatial variation impacts,” Journal of Astronomical Telescopes, Instruments, and Systems **7**, 038002 (Aug. 2021). Publisher: International Society for Optics and Photonics.

[40] Ichimoto, K., Lites, B., Elmore, D., Suematsu, Y., Tsuneta, S., Katsukawa, Y., Shimizu, T., Shine, R., Tarbell, T., Title, A., Kiyohara, J., Shinoda, K., Card, G., Lecinski, A., Streander, K., Nakagiri, M., Miyashita, M., Noguchi, M., Hoffmann, C., and Cruz, T., “Polarization Calibration of the Solar Optical Telescope onboard Hinode,” Solar Physics **249**, 233–261 (June 2008).

[41] White, A. J. and Harrington, D. M., “Modeling the polarization behavior of multi-layered mirror coatings for system-level polarization predictions of DKIST,” in [Advances in Optical and Mechanical Technologies for Telescopes and Instrumentation V], Geyl, R. and Navarro, R., eds., **12188**, SPIE, Montréal, Canada (Aug. 2022).

[42] Polyanskiy, M. N., “Refractive index database.” `https://refractiveindex.info`. Accessed on 2023-05-01.

[43] Boidin, R., Halenkovič, T., Nazabal, V., Beneš, L., and Němec, P., “Pulsed laser deposited alumina thin films,” Ceramics International **42**, 1177–1182 (Jan. 2016).

[44] Storn, R. and Price, K., “Differential Evolution – A Simple and Efficient Heuristic for global Optimization over Continuous Spaces,” Journal of Global Optimization **11**, 341–359 (Dec. 1997).

[45] Zielinski, K. and Laur, R., “Stopping Criteria for a Constrained Single-Objective Particle Swarm Optimization Algorithm,” Informatica **31**(1) (2007). Number: 1.

[46] Debenham, M., “Refractive indices of zinc sulfide in the 0.405–13-micron wavelength range,” Applied Optics **23**, 2238–2239 (July 1984). Publisher: Optical Society of America.

[47] "TFCalc (Software for Optical Thin Film) - HULINKS Inc.." `https://www.hulinks.co.jp/en/tfcalc-e`.

[48] Malitson, I. H. and Dodge, M. J., "Refractive Index and Birefringence of Synthetic Sapphire," in [Program of the 1972 Annual Meeting of the Optical Society of America], **62**, 1336, Journal of the Optical Society of America (1972).

[49] Elmore, D. F., Rimmele, T., Casini, R., Hegwer, S., Kuhn, J., Lin, H., McMullin, J. P., Reardon, K., Schmidt, W., Tritschler, A., and Wöger, F., "The Daniel K. Inouye Solar Telescope first light instruments and critical science plan," in [Ground-based and Airborne Instrumentation for Astronomy V], **9147**, 914707, International Society for Optics and Photonics (July 2014).

[50] Palik, E. D. and Ghosh, G., [Handbook of Optical Constants of Solids, Five-Volume Set: Handbook of Thermo-Optic Coefficients of Optical Materials with Applications], Elsevier Science & Technology, Saint Louis, UNITED STATES (1997).

[51] Hofmeister, A. M., Pitman, K. M., Goncharov, A. F., and Speck, A. K., "Optical Constants of Silicon Carbide for Astrophysical Applications. II. Extending Optical Functions from Infrared to Ultraviolet Using Single-Crystal Absorption Spectra," The Astrophysical Journal **696**(2), 1502 (2009).

[52] White, A. J. and Harrington, D. M., "Understanding polarization accuracy: the effect of mirror coating non-uniformity on instrument polarization," in [Advances in Optical and Mechanical Technologies for Telescopes and Instrumentation V], Geyl, R. and Navarro, R., eds., SPIE, Montréal, Canada (Aug. 2022).

[53] Gil, J. J. and Bernabeu, E., "A Depolarization Criterion in Mueller Matrices," Optica Acta: International Journal of Optics **32**, 259–261 (Mar. 1985).

[54] Gil, J. J. and Bernabeu, E., "Depolarization and Polarization Indices of an Optical System," Optica Acta: International Journal of Optics **33**, 185–189 (Feb. 1986).

[55] Chipman, R. A., "Depolarization index and the average degree of polarization," Applied Optics **44**, 2490 (May 2005).

[56] DeBoo, B., Sasian, J., and Chipman, R., "Degree of polarization surfaces and maps for analysis of depolarization," Optics Express **12**, 4941–4958 (Oct. 2004). Publisher: Optical Society of America.

[57] Sueoka, S. R., Polarization optical components of the Daniel K. Inouye Solar Telescope, PhD Thesis, The University of Arizona (2016). ISBN: 978-1-339-77830-3 Publication Title: ProQuest Dissertations and Theses.